3-9-2018

Patterns of Variation for the Sun and Sun-like Stars

Richard R. Radick
National Solar Observatory

G. Wesley Lockwood
Lowell Observatory

Gregory W. Henry
Tennessee State University

Jeffrey C. Hall
Lowell Observatory

Alexei A. Pevtsov
National Solar Observatory

Recommended Citation

Richard R. Radick et al 2018 ApJ 855 75

The Astrophysical Journal, 855:75 (28pp), 2018 March 10 https://doi.org/10.3847/1538-4357/aaaae3

Patterns of Variation for the Sun and Sun-like Stars

Richard R. Radick[1], G. Wesley Lockwood[2], Gregory W. Henry[3], Jeffrey C. Hall[2], and Alexei A. Pevtsov[4]
[1] National Solar Observatory, Sunspot, NM 88349, USA
[2] Lowell Observatory, Flagstaff, AZ, 86001, USA
[3] Center of Excellence in Information Systems, Tennessee State University, Nashville, TN 37209, USA
[4] National Solar Observatory, Boulder, CO, 80303, USA

Received 2017 December 7; revised 2018 January 19; accepted 2018 January 24; published 2018 March 9

Abstract

We compare patterns of variation for the Sun and 72 Sun-like stars by combining total and spectral solar irradiance measurements between 2003 and 2017 from the *SORCE* satellite, Strömgren *b*, *y* stellar photometry between 1993 and 2017 from Fairborn Observatory, and solar and stellar chromospheric Ca II H+K emission observations between 1992 and 2016 from Lowell Observatory. The new data and their analysis strengthen the relationships found previously between chromospheric and brightness variability on the decadal timescale of the solar activity cycle. Both chromospheric H+K and photometric *b*, *y* variability among Sun-like stars are related to average chromospheric activity by power laws on this timescale. Young active stars become fainter as their H+K emission increases, and older, less active, more Sun-age stars tend to show a pattern of direct correlation between photometric and chromospheric emission variations. The directly correlated pattern between total solar irradiance and chromospheric Ca II emission variations shown by the Sun appears to extend also to variations in the Strömgren *b*, *y* portion of the solar spectrum. Although the Sun does not differ strongly from its stellar age and spectral class mates in the activity and variability characteristics that we have now studied for over three decades, it may be somewhat unusual in two respects: (1) its comparatively smooth, regular activity cycle, and (2) its rather low photometric brightness variation relative to its chromospheric activity level and variation, perhaps indicating that facular emission and sunspot darkening are especially well-balanced on the Sun.

Key words: stars: activity – stars: solar-type – Sun: activity

Supporting material: figure set, machine-readable table

1. Introduction

1.1. Solar Activity and Variability

The solar atmosphere exhibits a variety of nonthermal phenomena collectively called activity. It is generally agreed that solar activity arises primarily in response to the generation, evolution, and annihilation of magnetic fields in the Sun's convective envelope and atmosphere. The most prominent magnetic structures in the solar atmosphere are the active regions, with their dark sunspots and surrounding bright faculae in the photosphere and overlying emission plages in the chromosphere. These active regions erupt and decay with lifetimes typically of a few months. As an active region ages, its spots disappear and its faculae disperse, merge with the magnetic network, and gradually disappear also. Nonradiative heating of the solar atmosphere above the faculae, both in active regions and in the network, is easily detected by the enhanced radiation it produces in chromospheric lines such as Ca II H+K and in coronal X-ray emission.

Many aspects of solar activity are accompanied by temporal variation; indeed, the word "activity" strongly suggests variability. In this paper, we will generally use the word "activity" when we wish to emphasize the nonthermal phenomena themselves—chromospheric emission, for example—and reserve the term "variability" to refer more narrowly to the temporal behavior of the phenomena. The archetypal temporal signature of solar activity is, of course, the quasi-cyclic variation in sunspot number, with a cadence of 8–13 years, which has now been observed since the 17th century. More generally, the solar cycle may be regarded as a variation in the number of active regions present on the Sun's surface. At cycle minimum, few active regions are present, and sometimes none at all. In contrast, at cycle maximum, there can be as many as 10 active regions present on the visible hemisphere of the Sun at one time.

Besides its signature variation in sunspot number, the solar cycle has also been detected as variations in the Sun's radiative outputs, beginning with the 10.7 cm radio flux some 70 years ago. In the 1970s, whole-disk observations to follow the variation of solar chromospheric Ca II K-line emission were begun at the National Solar Observatory (NSO; White et al. 1998; Scargle et al. 2013) that currently continue via the Integrated Sunlight Spectrometer (ISS) of the NSO's Synoptic Optical Long-term Investigations of the Sun (SOLIS) facility (Bertello et al. 2011). Starting in the late 1970s, variations in total solar irradiance (TSI) have been monitored by radiometers aboard a series of spacecraft, including the Total Irradiance Monitor (TIM) instrument on the *SOlar Radiation and Climate Experiment* (*SORCE*) satellite from 2003 to the present (Anderson & Cahalan 2005 and subsequent articles).

From these time series, we now know that the fractional amplitude of the solar cycle can reach ~15% in Ca II K-line emission. The corresponding amplitude of the TSI variation is much smaller, about 0.1%, marching in step with the sunspot number and integrated-disk Ca II emission. The variation of TSI is currently interpreted as a slight imbalance between the flux deficit produced by dark sunspots and the excess flux produced by bright faculae, with the facular effects dominating the competition on the decadal timescale of the solar cycle.

We conclude this brief review of solar activity and variability by presenting time series from 2003 through mid-2017 for the NSO 1 Å K-index equivalent width and *SORCE*/TIM TSI

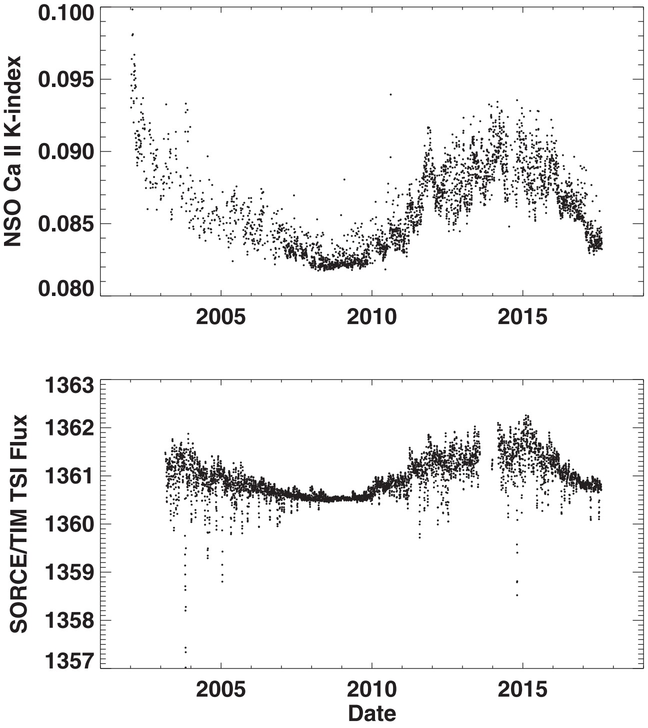

Figure 1. Solar time series from 2003 through mid-2017 for the NSO 1 Å K-index equivalent width (upper panel) and *SORCE*/TIM TSI (Wm^{-2}; lower panel).

(Figure 1). The direct correlation between chromospheric Ca II emission and TSI on the decadal timescale of the solar activity cycle is clearly evident. This pattern is also occasionally seen on shorter timescales: for example, near the end of 2011, there is a clear peak in the K-index coinciding with a less distinct peak in TSI, marking a prominent outburst of active region formation in October–December of that year.

We will return to these foundational data later in this paper when we examine the problem of placing the Sun in its stellar context.

1.2. Stellar Activity and Variability

Olin Wilson's discovery of activity cycles in cool main-sequence stars (Wilson 1978) launched the research field that has since become known as the "solar–stellar connection." Wilson monitored chromospheric Ca II H+K emission for almost 100 stars from 1966 to 1977. The Mount Wilson Observatory HK Program continued this work from 1977 through 2002 (Baliunas et al. 1995, 1998). Starting in 1992 and continuing to the present, similar Ca II H+K observations of the Sun and stars have been made at Lowell Observatory using the fiber-coupled Solar-Stellar Spectrograph (SSS; Hall & Lockwood 1995; Hall et al. 2007b, hereafter "H07").

Thanks largely to the observations pioneered at Mount Wilson, it is now recognized that the activity of a cool dwarf star is governed primarily by its mass and rotation rate, although chemical composition (Shapiro et al. 2015; Karoff et al. 2018) also plays a role. Young, rapidly rotating stars show strong activity that tends to vary irregularly in a complex, multi-timescale manner. In contrast, older, more slowly rotating stars (such as the present-day Sun) have considerably weaker activity that sometimes fluctuates irregularly, sometimes varies in a simple cyclic manner reminiscent of the solar cycle, and sometimes shows long-term uptrends, downtrends, or little variation at all (e.g., Egeland et al. 2017a). The timescales of stellar cycles range from a few years to more than a decade (Oláh et al. 2016). Among older stars, those more massive than the Sun tend to show low-amplitude variation, whereas those less massive than the Sun tend to show more pronounced cycles. The Sun currently has a relatively prominent activity cycle—indeed, judged simply by the appearance of its cycle as seen in the catalog published by Baliunas et al. (1995), the Sun looks more like a K-type star than an early G-type star (Figure 2).

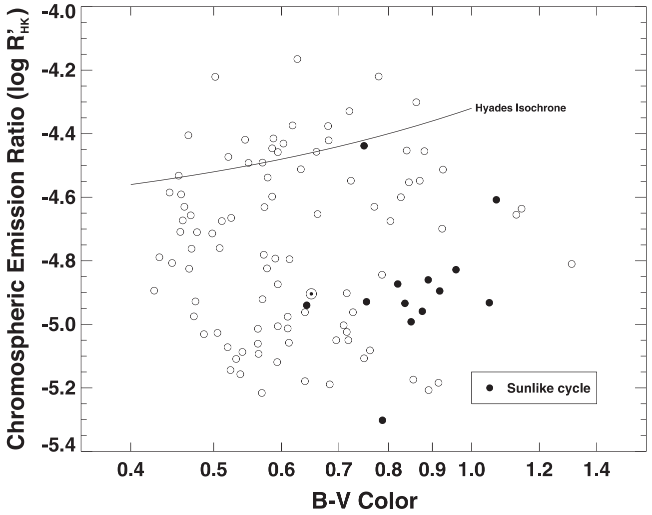

Figure 2. Stars of the Mount Wilson HK Program, displayed as a color–activity diagram. The Sun's location is also indicated. The ordinate measures, in logarithmic units, the fraction of a star's luminosity that appears as chromospheric H+K emission. Stars with simple Sun-like activity cycles are plotted with filled symbols; the 13 stars so selected are HD 3651, HD 4628, HD 10476, HD 16160, HD 26965, HD 32147, HD 81809, HD 103095, HD 152391, HD 160346, HD 166620, HD 201091, and HD 219834.

About 70 years ago, the Ca II H+K variability of stars now known as RS CVn binaries was explained in terms of emission from spatially limited stellar structures that might now be called stellar plages, an idea that subsequently was developed further to include the concept of starspots (Struve 1946; Eaton & Hall 1979). The variable components of the RS CVn systems are evolved stars whose strong activity is a consequence of rapid rotation enforced by tidal interaction with their nearby companions. As such, they do not represent particularly good solar analogs.

Somewhat closer solar analogs are another class of spotted stars, the BY Dra variables, which are young, rapidly rotating, low mass dwarf stars—typically K- and M-type stars (Kron 1950; Chugainov 1966; Torres & Ferraz Mello 1973). High-precision Strömgren *b*, *y* photometric studies of cool dwarf stars in the Hyades (1980–92) and Coma Berenices (1984–87) open clusters demonstrated that the BY Dra phenomenon extends to G- and late F-type stars rotating some 3× – 4× more rapidly than the Sun (Radick et al. 1990, 1995). The year-to-year photometric variability of these cluster stars in the visual continuum is typically some 20× greater than the cyclic TSI variation of the Sun, and exhibits the characteristic irregular temporal behavior shown by young stars in their chromospheric H+K emission.

These studies of young cluster stars inspired programs at the Lowell (1984–2000) and Fairborn Observatories (1993–2003) aimed at studying the long-term (year-to-year) Strömgren *b*, *y* photometric variability of a sample of 30+ stars whose chromospheric activity was being monitored regularly by the Mount Wilson HK program (Lockwood et al. 1997; Radick et al. 1998, hereafter R98; Lockwood et al. 2007, hereafter L07). The principal conclusions of this 20 year study were (1) on the year-to-year timescale and longer, both chromospheric H+K variability and photometric *b*, *y* variability among Sun-like stars are related to their average chromospheric activity by power laws. H+K variability decreases by a factor of about 4, and photometric variability by a full decade or more, from stars perhaps 10% solar age to Sun-age stars. The photometric variability of the Sun itself may be somewhat subdued for a star of its average activity level. (2) On these timescales, young active stars become fainter as their H+K emission increases. This implies that the year-to-year photometric variation of young stars is dominated by dark spots, in contrast to the Sun, whose net cyclic variation in TSI is driven by bright faculae. (3) Among older, less active, Sun-age stars, there is a preference for a pattern of direct correlation between photometric and chromospheric emission variations, not unlike the pattern between the TSI and K-index variations shown by the Sun (Figure 1). For these stars, however, the observed photometric variation tends to be close to the limiting precision of the observations, so this conclusion is more tentative.

Observations to monitor relatively bright stars very similar to the Sun (the so-called "solar analogs"; Cayrel de Strobel 1996) with the SSS at Lowell Observatory and automatic photometric telescopes (APTs) at Fairborn Observatory began in 1992 and 1993, respectively. Although the observing lists were initially uncoordinated, there was nonetheless considerable overlap. Combined results for 28 stars were reported in 2009 using time series 4–14 years in duration (Hall et al. 2009). Seven of these 28 stars overlapped the R98–L07 sample. The paper concluded that the Sun's low position in the activity–brightness plots of R98 and L07 is a selection effect. The present paper significantly increases both the stellar sample size and the observational duration of this 2009 study.

1.3. Comparing Solar and Stellar Measurements

The reader has perhaps noticed an apples-and-oranges issue in the preceding paragraphs: in discussing brightness variability, we described the Sun in terms of TSI, which is essentially a bolometric quantity, whereas we discussed stellar variability in terms of Strömgren *b*, *y* photometry, which is not bolometric. In the terminology of solar radiometry, Strömgren *b* (469 nm, FWHM 20 nm) and Strömgren *y* (548 nm, FWHM 22 nm) are species of spectral irradiance, and although they are located near the peak of the solar energy distribution, there is no a priori reason to suppose that $(b + y)/2$ (the photometric quantity we used to study the variability of Sun-like stars in previous papers) varies directly with TSI for the Sun. In fact, we implicitly made that assumption in our earlier papers, and estimated factors for scaling small changes in TSI to changes in solar $(b + y)/2$ based on both a simple blackbody analysis as well as measurements from the Variability of solar IRradiance and Gravity Oscillations (VIRGO) experiment aboard the *SOlar and Heliospheric Observatory* (*SOHO*) satellite (R98). This assumption was thrown into doubt several years ago when measurements of spectral solar irradiance (SSI) from the Spectral Irradiance Monitor (SIM) instrument aboard *SORCE* appeared.

The gist of these results (e.g., Harder et al. 2009; Haigh et al. 2010) is that from 2004 through 2007, during the declining phase of solar cycle 23, SSI integrated in the 400–700 nm band (accounting for about 39% of the TSI) increased by about 0.5 $\mathrm{W m^{-2}}$ (about 0.1%), mainly in 2004. In the narrower Strömgren *b* and *y* bands, the integrated increases were about zero and 0.06 $\mathrm{W m^{-2}}$, respectively. At the same time, TSI decreased by about 0.4 $\mathrm{W m^{-2}}$.

Apparently, either the Sun or *SORCE*/SIM was not behaving as expected from 2004 through 2007. Appeals to models did little to clarify the matter. On the one hand, a solar irradiance model calibrated using ground-based image measurements between about 1988 and 2010 from the San Fernando Observatory (Preminger et al. 2011) indicated a change of about 0.02 $\mathrm{W m^{-2}}$ in visual continuum brightness in bands at 472 and 672 nm, anticorrelated with changes in solar activity, thereby tending to confirm *SORCE*/SIM. On the other hand, multicomponent empirical models of SSI (Lean 2000; Ball et al. 2011) arrived at the contrary conclusion, indicating a change of about 0.2% in the 400–700 nm band, in step with the solar cycle. A theoretical study using 3D MHD simulations (Criscuoli & Uitenbroek 2014) suggested that either correlated or anticorrelated behavior could be obtained, depending on the detailed assumptions adopted for facular radiance and magnetic flux. In contrast to the mixed picture from models, annual means of Sun photometer measurements for 2002–2012 from *SOHO*/VIRGO provide evidence that SSI in the 500 nm band, midway between Strömgren *b* and *y*, does, indeed, vary directly with TSI on the decadal timescale (Wehrli et al. 2013), contrary to the *SORCE*/SIM result.

A more recent paper (Woods et al. 2015) sidestepped addressing the Sun versus instrument issue directly by examining instead irradiance variations during six-month intervals—"outburst periods"—typical of active region growth and decay, but arguably short enough to minimize the effect of instrumental drift. An analysis of energy excesses and deficits led to the conclusion that SSI varies directly with TSI on the outburst timescale across the entire spectral range of *SORCE*/SIM (240–1600 nm), except in the 1400–1600 nm band, where the variations are out of phase. This out-of-phase behavior in the near-infrared (NIR) was not unexpected, because the facular contrast is known to be negative in the NIR near 1.63 μm (Foukal et al. 1990). In particular, the out-of-phase variations in the 400–700 nm band found previously were not seen on the outburst timescale. If the solar cycle is presumed to be the superposition of many individual active region outbursts, the implicit implication of this study is that the intrinsic (i.e., solar) cyclic variation of SSI in the visual continuum is, in fact, in step with the TSI variation, and that Strömgren *b* and *y* most likely also vary directly with TSI on the timescale of the solar cycle.

In 2017 May, a new release of the *SORCE*/SIM SSI data, version 23, appeared to reverse the earlier results, indicating that SSI in the visual continuum does, indeed, tend to follow TSI on the year-to-year timescale of the solar cycle. We will examine this matter in considerably greater depth in Section 4.2 of this paper.

In contrast to the photometric situation, the comparison of solar and stellar measurements of chromospheric emission has been relatively uncontroversial, albeit challenging in detail (e.g., H07; Egeland et al. 2017b). The difficulties associated with expressing solar and stellar activity measurements in absolute physical units has led to the widespread use of instrumental indices, such as the Mount Wilson S-index and the NSO 1 Å K-index, which offer the powerful attraction of internal self-consistency. This advantage is offset, however, by two inescapable drawbacks: (1) such indices are tightly tied to the instruments used for their definition, and any change in instrumentation inevitably involves uncertainties of intercalibration, and (2) intercomparison among stars with different physical characteristics can be uncertain because stellar characteristics (primarily temperature, but also metallicity and surface gravity) that affect the spectral features that specify an index also become entangled in its interpretation—i.e., an index is not a clean diagnostic of magnetic activity when comparing physically dissimilar stars.

The alternative is to express stellar activity measurements in surface flux units. Middelkoop (1982) and Rutten (1984) took early steps in this direction by defining a transformation from the Mount Wilson S-index to arbitrary flux units that both removes a color (i.e., temperature)-dependent effect from the S-index and breaks out explicitly the dependence of the surface flux on stellar effective temperature. Although neither author cites a number, the uncertainty implicit in this transformation appears to be about ±10%. The further transformation of this arbitrary flux unit to absolute surface flux introduces an additional uncertainty (e.g., from angular diameters); this is discussed by H07, who state that the cumulative uncertainty involved in the process of converting the instrumental S-index to physical flux units can amount to as much as 25%.

Uncertainty also arises from the fact that not all of the intensity measured by an instrumental quantity such as the 1 Å K-index arises from chromospheric emission. The assumption that all of the intensity within (and none outside) the K_1 minima is chromospheric emission is perhaps not strictly correct, but it is the usual basis for a further empirical correction for non-chromospheric—i.e., photospheric—emission (Hartmann et al. 1984; Noyes et al. 1984; H07). The most widely used version of this correction, based on spectra of three stars plus the Sun, is not likely to be more accurate than ~10% (Hartmann et al. 1984).

The end product of this is the widely used chromospheric emission ratio R'_{HK} (Noyes et al. 1984), which ostensibly measures the fraction of a star's luminosity that appears as chromospheric H+K emission. The uncertainties described above, in conjunction with the typical errors associated with the S-index (1%–2%) and Johnson B, V photometry (also 1%–2%), the inputs for the transformation, suggest that any value cited for R'_{HK} is uncertain by at least 15% (~0.06 dex).

Attempts to further break down chromospheric emission into variable and non-variable components (or, more controversially, into magnetic and non-magnetic components; e.g., Schrijver 1995; Judge et al. 2003; H07) have led to the concepts of an underlying, invariable "basal" chromosphere as well as the excess chromospheric flux that excludes emission from it. We note, however, that Pevtsov et al. (2013) suggest that the basal chromosphere may not be strictly unvarying on the Sun, but rather exhibits a slight (~6%) variation in phase with the sunspot cycle. In terms of the active region paradigm for solar (and stellar) activity on the timescale of the solar activity cycle that we have suggested above, the excess flux includes all contributions to chromospheric emission that arise from active regions or their decay products in the active network, and the basal chromosphere may include both non-magnetic (i.e., acoustic) and magnetic (i.e., quiet network) sources.

In this paper, we will generally follow historical precedent and use either the S-index or R'_{HK} units to express chromospheric activity, despite their shortcomings. The many issues we mention above certainly comprise a subject ripe for revisiting and revision, but that is something beyond the scope of the present paper.

1.4. Objectives and Outline of the Present Paper

The objectives of the present paper are to augment the analyses of earlier papers, using a sample of 72 more or less Sun-like stars observed with both the Lowell Observatory SSS instrument and the Fairborn Observatory APTs, and to place the Sun as accurately as possible into this stellar context. Our 72 star sample is a superset of the 28 stars studied by Hall et al. (2009), and it is considerably more "Sun-like" in its characteristics than the R98–L07 sample. Eighteen stars are in common with the R98–L07 sample, and 39 are in common with the Mount Wilson HK program stars.

Design improvements incorporated in the Fairborn photometers, up to 10× more numerous observations per season, larger telescopes, and better procedures for comparison star selection combine to offer higher precision photometry (perhaps 5× better) on the year-to-year timescale than previously obtained from Lowell Observatory. Because the amplitude of the photometric variability of solar-age Sun-like stars is expected to be on the order of 0.1%, high precision is critically important.

In Section 2 of this paper, we will discuss the stellar sample and the instrumentation and observations. Section 3 will describe the analysis of the stellar time series and present time series plots for selected stars. Section 4 will return to the issue of placing the Sun in its stellar context with a detailed examination of the relationship between TSI and Strömgren b, y photometric variability on the decadal timescale. In Section 5, we will present our results, primarily: (1) the relationships between chromospheric H+K emission variability, photometric variability, and average chromospheric activity, and (2) the patterns of correlation between photometric and chromospheric variability as a function of stellar color and average activity. Section 6 will be a summary.

2. Stellar Sample, Instrumentation, and Observations

2.1. Stellar Sample

As mentioned previously, observations to monitor relatively bright stars very similar to the Sun (spectral type late-F through G, unevolved or, at most, slightly evolved) have been made with the SSS at Lowell Observatory and APTs at Fairborn Observatory beginning in 1992 and 1993, respectively. In all, 72 stars, including 18 from the broader R98–L07 sample, have been observed at both locations, some for as long as 24 seasons. These joint observations provide the primary stellar data for this paper.

In terms of the three-level taxonomy for stars resembling the Sun defined by Cayrel de Strobel (1996) and subsequently quantified by Soderblom & King (1998), these stars, except for some inherited from R98–L07 and an additional rogue or two, are "solar-like" stars (or, as Soderblom and King prefer, perhaps more grammatically, solar-type stars)—originally defined as “a very broad class of stars, in which are found a mixture of late F, early, middle, and, sometimes, late G type dwarfs and sub-giants.” Some 55 of these stars also satisfy the narrower criteria for “solar-analog” stars, originally defined as “unevolved, or slightly evolved Pop I disk stars with effective temperatures, degree of evolution, metallicities, and kinematic properties not very different from those of the Sun.” This was subsequently quantified as stars having temperature within ~500 K of the Sun (i.e., $B - V$ color between about 0.52 and 0.82, or spectral type between F7 and K0), and lying within one magnitude of the Zero-Age Main Sequence (ZAMS). Finally, several stars in our sample have been singled out at one time or another as “solar twins,” including HD 146233 = 18 Sco (Porto de Mello & da Silva 1997) and eight of the “Top Ten” solar analogs from ELODIE (Soubiran & Triaud 2004; although, according to the strictest definition of Soderblom & King, no “solar twins” are known). In general, we will use the somewhat less specific adjective “Sun-like” to describe our present sample, rather than force-fitting it into the three-level definitional scheme just described.

Table 1 presents the demographics of our 72 stars, plus the Sun. The primary purpose of this table is to identify the stars of our sample and document the values that we adapted for our analysis, rather than provide an authoritative, comprehensive compilation of activity-related stellar parameters. Accordingly, we do not tabulate data (e.g., metallicity, stellar rotation, or stellar cycle periods) that do not enter into the presentation of our work in a material way. The V magnitudes and $B - V$ colors are from the *Hipparcos I Catalogue* (ESA 1997), and should reflect the internal consistency of that source. In contrast, the entries for spectral type have been extracted from the heterogeneous data contained in the VizieR and SIMBAD databases, and are presented principally because we tend to discuss stars in terms of that parameter.

The first five columns of the table are self-explanatory. Column 6 lists values for log R'_{HK} (Noyes et al. 1984), which measures, in logarithmic units, the fraction of a star’s luminosity that appears as chromospheric H+K emission. These values were computed using the $B - V$ colors from column 4 and long-term SSS S-indices from this work (Table 3, column 4, below), and therefore should be relatively self-consistent. Column 7 lists values for a metric previously devised (R98) to quantitatively assess a star as a solar analog by measuring its distance from the Sun in a three-dimensional M_V, $B - V$, log R'_{HK} manifold, weighting equally distances of 1.0 mag in M_V, 0.1 mag in $B - V$ and 0.2 in log R'_{HK} (about 0.05 in the Mount Wilson S-index). In the R98 and L07 studies, the closest matches to the Sun according to this metric were over a unit away. In contrast, 30 stars of the present sample are less than one unit distant from the Sun, and the closest, HD 146233, is only 0.13 unit away, confirming its status as a “solar twin.” The final column identifies stars that were included in previous studies: E = ELODIE, H = H07, L = L07, and M = Mount Wilson HK program.

Figure 3 presents two HR diagrams. The upper panel shows the stars of the Mount Wilson HK program, along with the Sun, with the 32 star subset studied by L07 represented by filled circles. The lower panel shows the stars of the present sample, along with the Sun, with the 18 stars in common with the L07 study represented by filled circles. Reverting to Cayrel de Strobel’s taxonomy for a moment, the concentration of “solar analog” stars surrounding the Sun is evident in the lower panel, as well as the relative absence of such stars in the L07 sample shown in the upper panel. We might also remark that we use a logarithmic scale to plot $B - V$ color in this figure and more generally throughout this paper, simply to reduce the pile-up of stars on the left side of the diagrams.

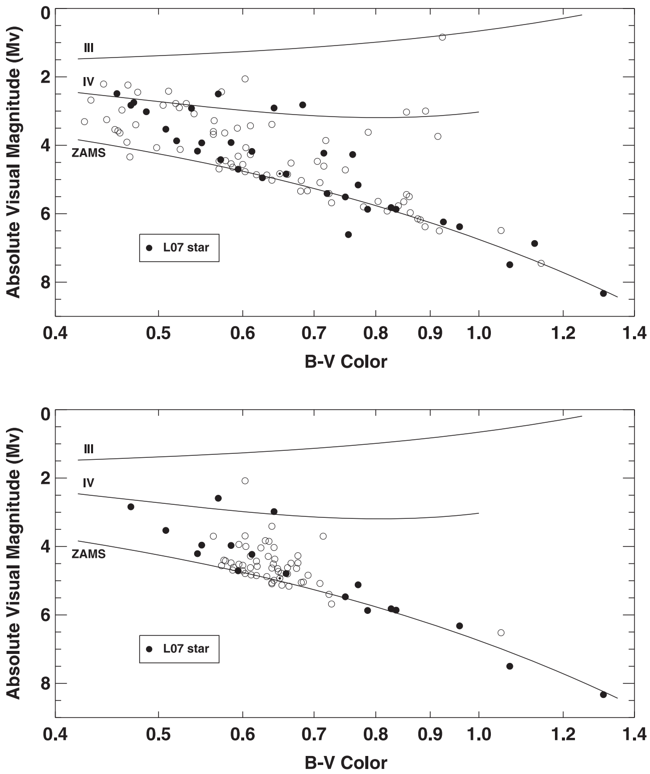

Figure 3. HR diagrams for the stellar samples studied by the Mount Wilson HK Program and Lockwood et al. (2007, L07; upper panel), and the present sample of 72 stars and the 18 stars in common with L07 (lower panel).

2.2. Photometric Instrumentation and Data Acquisition

Beginning in 1993, three APTs at Fairborn Observatory have accumulated precision Strömgren b, y photometric data for nearly 300 Sun-like stars. Several other APTs monitor exoplanet targets. The APTs typically produce 50 or more nightly observations for each target each year. Henry’s (1999) comprehensive account describes the hardware, software, telescope control system, differential photometry observing scheme, data quality control metrics, and nightly performance diagnostics. Two recent papers (Judge et al. 2012; Lockwood et al. 2013) validate the conservative experimental design and consistent data management procedures in characterizing the 20 year millimagnitude level stellar variability demographics for more than 150 Sun-like stars. These papers show that levels of stellar variability as low as the Sun’s cyclic TSI variation can, under favorable circumstances, be detected. This fills in a low-level variability regime only partially explored in the sparse and less precise sampling available from the earlier Lowell work conducted with a single smaller telescope.

The Fairborn observational design follows the Lowell recipe: single program stars and three nearby comparison stars form

Table 1
Stellar Sample

HD	V	M_V	$B-V$	Spectral Type	Log $R'_{\rm HK}$	Metric	Notes
Sun		4.83	0.640	G2V	−4.92	0.00	
1461	6.47	4.64	0.674	G3V	−5.04	0.68	H
1835	6.39	4.79	0.659	G2.5V	−4.48	2.21	H, L, M
4307	6.15	3.69	0.603	G0V	−5.20	1.84	H
6920	5.67	2.08	0.603	F9IV	−4.83	2.82	M
9562	5.75	3.40	0.639	G1V	−5.20	1.99	M
9986	6.77	4.73	0.648	G2V	−4.79	0.68	
10145	7.70	4.84	0.691	G5V	−4.95	0.52	E
10307	4.96	4.43	0.618	G1V	−5.01	0.61	E, H
10476	5.24	5.86	0.836	K1V	−4.97	2.23	L, M
10700	3.49	5.68	0.727	G8V	−4.95	1.22	H, M
13043	6.88	4.04	0.624	G2V	−5.01	0.92	
13421	5.64	2.59	0.569	G0IV	−5.23	2.79	L, M
18256	5.58	2.84	0.471	F6V	−4.81	2.68	L, M
19373	4.05	3.94	0.595	F9.5V	−5.02	1.11	
20630	4.84	5.04	0.681	G5V	−4.44	2.48	H, M
30495	5.49	4.87	0.632	G2.5IV-V	−4.51	2.09	H, M
32147	6.22	6.52	1.049	K4V	−4.97	4.43	
35296	5.00	4.21	0.544	F8V	−4.42	2.77	H, L, M
38858	5.97	5.06	0.639	G2V	−4.89	0.29	H
39587	4.39	4.70	0.594	G0V	−4.41	2.61	H, L, M
42618	6.85	4.99	0.642	G4V	−4.96	0.25	E
42807	6.43	5.16	0.663	G5V	−4.47	2.33	H
43587	5.70	4.28	0.610	G0V	−4.99	0.71	H, M
50692	5.74	4.56	0.573	G0V	−4.96	0.74	
52711	5.93	4.52	0.595	G0V	−4.96	0.57	
55575	5.54	4.40	0.576	F9V	−4.95	0.78	
72905	5.63	4.84	0.618	G0.5V	−4.37	2.76	M
75332	6.22	3.96	0.549	F7V	−4.61	2.03	L, M
76151	6.01	4.81	0.661	G2V	−4.69	1.18	H, M
78366	5.95	4.53	0.585	G0IV-V	−4.64	1.57	M
81809	5.38	2.96	0.642	G1.5IV-V	−4.98	1.89	L, M
82885	5.40	5.12	0.770	G8Va	−4.69	1.76	H, L, M
86728	5.37	4.48	0.676	G4V	−5.13	1.15	
88986	6.46	3.85	0.635	G2V	−5.22	1.77	H
89269	6.66	5.13	0.653	G6V	−5.03	0.62	E
90508	6.42	4.62	0.610	G0V	−5.06	0.75	H
95128	5.03	4.29	0.624	G1V	−5.06	0.89	E, H
97334	6.41	4.71	0.600	G1V	−4.45	2.43	H, M
101364	8.67	4.65	0.647	G0V	−4.97	0.31	
101501	5.31	5.40	0.723	G8V	−4.53	2.23	H, M
109358	4.24	4.61	0.588	G0V	−4.97	0.61	
115043	6.82	4.80	0.603	G1Va	−4.49	2.19	M
115383	5.19	3.97	0.585	G0IV	−4.46	2.54	H, L, M
115617	4.74	5.08	0.709	G7V	−4.99	0.80	M
117176	4.97	3.70	0.714	G5V	−5.26	2.16	
120066	6.33	3.83	0.630	G0V	−5.14	1.47	
120136	4.50	3.53	0.508	F7IV-V	−4.75	2.06	H, L, M
126053	6.25	5.07	0.639	G1.5V	−4.94	0.26	M
140538	5.86	5.03	0.684	G2.5V	−4.74	1.04	H
141004	4.42	4.00	0.604	G0-V	−4.97	0.93	M
143761	5.39	4.21	0.612	G0+Va	−5.09	1.08	H, L, M
146233	5.49	4.77	0.652	G2Va	−4.93	0.13	E, H
149661	5.77	5.82	0.827	K0V	−4.71	2.37	L, M
152391	6.65	5.47	0.749	G8.5V	−4.45	2.68	L, M
154417	6.00	4.42	0.578	F9V	−4.50	2.26	M
157214	5.38	4.60	0.619	G0V	−5.01	0.53	H
159222	6.52	4.63	0.639	G1V	−4.89	0.25	
160346	6.53	6.32	0.959	K2.5V	−4.82	3.56	L, M
168009	6.30	4.51	0.641	G1V	−4.99	0.46	E, H
181655	6.29	4.27	0.676	G5V	−4.97	0.71	
185144	4.67	5.87	0.786	G9V	−4.83	1.86	L, M
186408	5.99	4.37	0.643	G3V	−5.07	0.88	
186427	6.25	4.62	0.661	G3V	−5.04	0.65	E
187691	5.12	3.70	0.563	F8V	−5.10	1.61	M

Table 1
(Continued)

HD	V	M_V	B–V	Spectral Type	Log $R'_{\rm HK}$	Metric	Notes
187923	6.16	4.03	0.642	G0V	−5.05	1.01	
190406	5.80	4.55	0.600	G0V	−4.77	0.90	H, M
197076	6.43	4.82	0.611	G1V	−4.89	0.34	H
201091	5.20	7.49	1.069	K5V	−4.61	5.28	L, M
201092	6.05	8.33	1.309	K7V	−4.90	7.55	L, M
206860	5.96	4.70	0.587	G0V	−4.43	2.53	M
217014	5.45	4.48	0.666	G2IV	−5.09	0.93	M
224930	5.80	5.37	0.690	G5Vb	−4.92	0.74	M

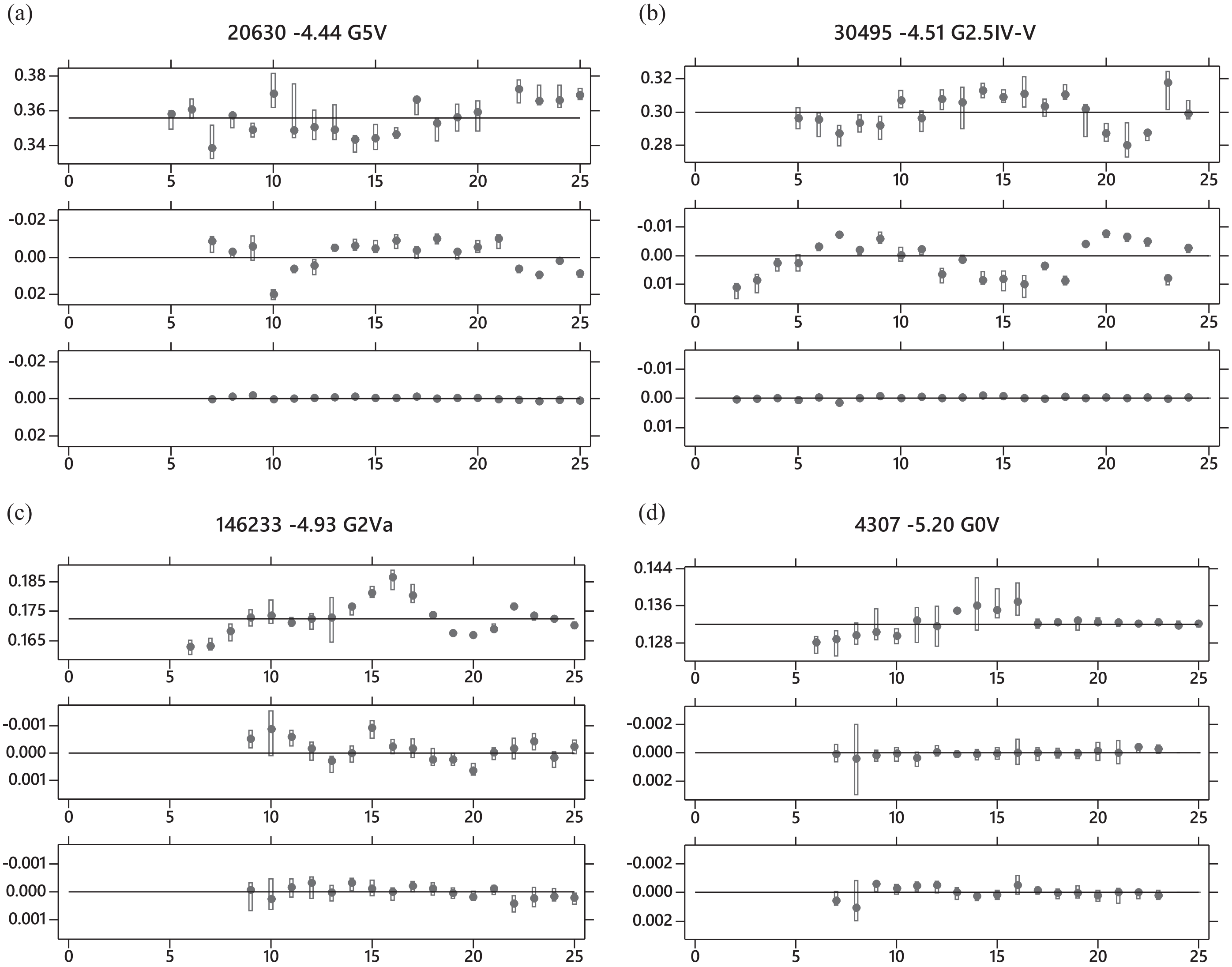

Figure 4. (a) Stackplot of Ca II H+K S-index and $(b + y)/2$ seasonal values for consecutively numbered seasons 1 (1992–1993) to 25 (2016) for HD 20630, a very active star. The upper panel shows the median S-index (filled circles) and 95% confidence intervals (rectangular boxes). The center panel shows $(b + y)/2$ seasonal tri-mean differential magnitudes of the program star, relative to the average of two comparison stars, with brightness increasing upward, and 95% confidence intervals (rectangular boxes). The bottom panel shows the seasonal tri-mean differential $(b + y)/2$ magnitude of the comparison stars, reduced by $\sqrt{2}$ to make the appearance of the comparison star variability visually commensurate with the program star variability shown in the center panel, and 95% confidence intervals (rectangular boxes). (b) Stackplot for HD 30495, a moderately active star. (c) Stackplot for the "solar twin" HD 146233 (18 Sco), a relatively inactive star. (d) Stackplot for HD 4307, a very inactive star.

(The complete figure set (72 images) is available.)

quartet groups for differential photometry. The lore of low-level stellar variability across the HR diagram (e.g., Grenon 1993, Figure 4) illustrates the challenge: our targets and their comparison stars all lie in the least variable part of the HR diagram. Prior photoelectric photometry of open clusters at Lowell in the 1980s (Hyades: Lockwood et al. 1984;

Radick et al. 1987, 1995, and Coma Berenices: Radick et al. 1990) and earlier field star variability results (Jerzykiewicz & Serkowski 1966) exposed the limitations of the technique. The principal conundrum is that we seek to characterize variability among Sun-like stars using comparison stars that are themselves likely to be variable. Learning from the Lowell work, the Fairborn experimental design sought to improve the odds of success by selecting F-type comparison stars that on average seem likely to be less variable than the more Sun-like target stars, at the cost of increased risk of color-dependent instrumental effects (which, in retrospect, have not materialized).

The four stars in a quartet yield six pairwise differential magnitudes for each filter, the least variable two comparison stars setting the baseline noise level for the quartet. Using these two comparison stars, we obtain estimates of the gross (upper limit) rms variability of the program star for each season plus a precisely determined measure of comparison star variability (observational plus intrinsic). In Section 3, we will describe how we extract estimates of intrinsic variability for the program stars themselves.

2.3. Spectroscopic Instrumentation and Data Acquisition

Using the fiber-fed SSS at Lowell Observatory's 1.1 m telescope, we have accumulated thousands of solar and stellar spectra for more than 100 targets since 1992 in monthly observing runs that typically yield a dozen or more measurements of Ca II H+K emission and the nearby reference continuum per season per target. Stellar spectra use the full aperture of the telescope, whereas sunlight comes from a 0.2 mm optical fiber solar feed. Since sunlight and starlight follow the same optical path through the spectrograph, the comparison of solar and stellar spectra is straightforward. Hall & Lockwood (1995) described the initial program, and subsequent papers have presented results from various aspects of this long-term program (e.g., Hall et al. 2007a, 2009; Egeland et al. 2015; Egeland 2016; Egeland et al. 2017b). The primary data product of this project is the S-index of Ca II H+K emission.

The SSS instrument resides in a dust-tight enclosure in a small room, mechanically isolated on a pier separate from the telescope. Although air conditioning and heating attempt to maintain "room temperature" year round, records show fluctuations of some ±2.5 °C, with occasional excursions as large as 5°–8°. After installation in the late 1980s, the focus and other optical alignments were never changed except when the CCD cameras were replaced in 2008. The mapping of the H+K spectral region onto the camera pixels is thus fixed except for radial velocity offsets. White-light flat-field illumination fed by the same fiber optics provides the customary pixel-to-pixel gain calibration. Nonlinear effects are thought to be negligible. Exposure depth can vary, however, owing to sky transparency, seeing, and observer selection of exposure time.

The SSS data divide into two epochs: 1992–2008 (the original TeK CCD camera, "CCD-1") and 2008–2016 (a new Andor CCD camera, "CCD-2"), the latter providing better quantum efficiency and 10× lower read noise. Data review showed that CCD-2 satisfactorily reproduces the original Mount Wilson S-index but also revealed a small offset between CCD-1 and CCD-2 (Egeland et al. 2017b), subsequently compensated in data reduction. Inspection of the much more numerous solar spectra further shows that data from 1992–2003 are noticeably noisier with respect to spectral line position and intensity fluctuations than observations from 2004–2007. Solar observations taken after 2008 with CCD-2 are even better than the 2004–2007 data with respect to both intensity fluctuations and stability of line positions relative to the camera pixels.

3. Analysis and Results

3.1. Photometric Data Validation and Analysis

The three robotic telescopes at Fairborn Observatory that provided data for this paper ("T4," "T8," and "T11") are programmed to operate whenever they can find stars, which leads to data acquired under nonphotometric conditions. We have therefore had to develop robust semi-automated procedures to remove bad observations, as will be described below.

The APT "T4" is equipped with a single-channel photometer that measures Strömgren *b* and *y* sequentially. The APTs "T8" and "T11" have dual-channel photometers that measure *b* and *y* simultaneously using dichroic beamsplitters, thereby both increasing throughput and slightly improving photometric precision by speeding up the observational cadence.

A nightly APT observation for a quartet produces three cycles of six pairwise differential magnitudes for each filter, *b* and *y*. The first step of data validation is to apply a "cloud filter": if the cycle-to-cycle standard deviation of any of the 12 pairwise differential magnitudes exceeded a threshold value, that quartet observation was discarded. We ultimately adopted a cloud filter threshold of 0.005 mag, roughly equivalent to the point where an experienced manual observer would quit. Cloud filter screening at the 0.005 mag level eliminates 20%–40% of data, but our experience showed that ruthless early vetting minimized difficult decisions later in confronting outliers, one by one, in a manner that might be less objective and certainly more laborious.

For plotting and tabulation convenience, we subtracted the grand mean from all of the differential magnitude data series. Then, using an interactive brushing technique in the Minitab Statistical Software that we used for all of the post-observation photometric data analysis, we removed the worst outliers. A few rounds of this procedure usually brought the range of remaining outliers within ∼0.01 mag of the central mass of points. This typically left only a few discrepant points remaining in the dubious realm of nominally acceptable photometry that nonetheless seemed unlikely to reflect intrinsic variability in our sample of quiescent Sun-like stars.

What remained after this process were annual batches of nightly data points for which we had to determine an optimum measure of central tendency. After some experimentation with robust estimators (Rosenberger & Gasko 1982), we adopted the tri-mean as a conservative hedge against fat-tail outliers. In this regard, the tri-mean, defined as

$$1/4(\text{first quartile}) + 1/2(\text{median}) + 1/4(\text{third quartile}),$$

is more forgiving than the traditional straight mean and has a slightly higher efficacy than the simple median. Nonetheless, in our analysis, we also computed traditional means for comparison with the tri-means. Significant differences rarely appeared.

The end products of this process are values for the annual (i.e., seasonal) brightness for each star. Because Sun-like stars rarely have rotation periods longer than the Sun's 27 days or, perhaps more strictly, tend not to exhibit measurable rotational brightness modulation if they are rotating more slowly than the Sun (e.g., McQuillan et al. 2014), our procedure of collapsing our photometric observations into a single annual value should effectively suppress rotational effects and ensure that the measured inter-annual variability reflects primarily phenomena due to active region evolution.

As an aside, it seems likely that the nightly APT photometry would yield rotation periods, at least for the more active stars in our sample, and the SSS data would also, at least from the CCD-2 era after 2008. A rule of thumb developed from experience many years ago (e.g., Radick et al. 1995) suggests that one needs at least 30 observations per season with a signal-to-noise ratio of at least 2–3 for the Lomb–Scargle periodogram algorithm to work reliably for rotation analysis, and the nightly data underlying this paper certainly satisfy these conditions in many cases. Likewise, with up to 24 seasons of data, an investigation of cycle periods might be fruitful. However, such analyses are beyond the scope we have set for this paper; we leave that fruit on the tree for later harvest, perhaps by others.

3.2. Photometric Results

We extracted the net intrinsic program star variation (i.e., variation compensated for comparison star variability) as follows (L07):

$$s_1^2 = \sigma^2{}_{1,23} - 1/2\,\sigma^2{}_{2,3} - \varepsilon^2, \qquad (1)$$

where $s_1{}^2$ is the intrinsic program star variance, $\sigma^2{}_{1,23}$ is the observed variance of the program star (“1”) minus the mean of the two comparison stars (“2” and “3”), $\sigma^2{}_{2,3}$ is the observed variance of the comparison star pair, and ε^2 is a small baseline “instrumental” noise variance.

The first two terms on the right-hand side are unbiased measured quantities that nevertheless include some uncertainty since they are based on a set of annual tri-means. The final term, ε^2, is an estimate of measurement noise based on the lower bound of the distribution of comparison star variances. The values we adopted are $\varepsilon = 0.00021$ mag for the APT T4 (46 stars in this paper), 0.00014 mag for T8 (23 stars), and 0.00014 mag for T11 (3 stars). We believe that this term represents the measurement error when there is no sensible variation in the target stars; presumably it reflects scintillation and atmospheric transparency fluctuations as well as Poisson noise, but we have not analyzed its exact origin. For comparison, earlier Lowell photometry with similar technique but a smaller telescope yielded $\varepsilon = 0.00060$. For most stars, the ε^2 term has a negligible effect on the net variation calculation. Statistically, the purpose of ε^2 is to ensure that Equation (1) is an unbiased estimator for program star variation. This means that, for a large sample of non-varying program stars, Equation (1) should deliver a set of values for $s_1{}^2$ that are distributed around zero, with positive and negative values equally likely. We will return to this point in Section 5.

Variability results for the 72 stars are shown in Table 2. The first line in each set of rows gives the observed gross standard deviations of the N seasonal tri-mean values of the program star minus the mean of the best two comparison stars ($\sigma_{1,23}$). The second row gives the corresponding values for one comparison star minus the other ($\sigma_{2,3}$), and the third row the net intrinsic program star variation (s_1), calculated using Equation (1), above. Twelve stars yielded a negative net variance in b, y, or $(b+y)/2$, indicating that the comparison star variability overwhelmed any program star variation. A fourth row entry, when present, gives corresponding values from L07.

3.3. Spectroscopic Results

A pipeline IDL-based reduction procedure applied equally to all SSS spectra performed continuum fitting and extraction of Ca II emission, resulting in the S-index as the fundamental output for each spectrum (Hall et al. 2007b). The data included in this study were recently re-processed through an automated procedure that assures consistency from star to star and year to year. Both $B-V$ and $b-y$ colors are required to produce the S-index (Egeland et al. 2017b). The colors used for processing the SSS spectra were obtained as follows: for $B-V$, Johnson et al. (1966) or, if that was unavailable, Eggen (1986). That covered almost all the stars. Likewise, for $b-y$, Olsen (1993, 1994a, 1994b) was the source for the vast majority of our sample. If that was not available, we used Hauck & Mermilliod (1998).

Table 3 gives the results of the Lowell SSS measurements. The date range is the total span of the measurements, $N_{n>5}$ is the number of seasons used for regressions of seasonal mean $(b+y)/2$ mag on S-index, further discussed in Section 5. The final columns of Table 3 give the slopes of those regressions and their standard errors. These slopes provide the essential relationship between brightness and chromospheric variation over a wide range of log $R'_{\rm HK}$; they undergo a sign reversal from negative to positive as we move from spot-dominated active stars to facula-dominated stars like the Sun.

3.4. Electronic Data

Seasonal data for all the stars in this study are available as a machine-readable table. Table 4 describes the contents of each field in the electronic file. To facilitate machine reading using IDL, Fortran, Excel, etc. and also to highlight missing seasons in the 25 year coverage time span, 25 data lines for each star are provided even when some seasons have no data. All of the photometric data tabulated and shown on the plots described in the next section have had their grand means subtracted, to center the ensemble of values on zero.

3.5. Stellar Time Series

Figure 4 shows the Ca II H+K S-index and photometric variation for a representative sample of four stars, arranged in order of decreasing mean log $R'_{\rm HK}$. Each plot contains three panels: (1) seasonal median SSS S-index, (2) seasonal tri-mean APT $(b+y)/2$ program star differential magnitude relative to the best pair of comparison stars, with brightness increasing upward, and (3) seasonal tri-mean $(b+y)/2$ differential magnitude of that best comparison star pair, reduced by $\sqrt{2}$ to make the appearance of the comparison star variability visually commensurate with the program star variability shown in the center panel. Each symbol is a composite of the seasonal median (SSS) or tri-mean (APT) and its enclosing 95% confidence interval. The horizontal scale, identical for each star, comprises 25 consecutive seasonal data batches starting from 1992–1993 (“1”) to 2016 (“25”); this convention was dictated by the software used to produce the plots. Because each season’s observations center approximately on opposition, the horizontal scale is very nearly a linear timescale, and the plots are nearly equivalent to traditional light curves with their explicit time axes. The data series for the photometry have

Table 2
Photometric Results

HD	HD Comp2	HD Comp3	Tel	N_{years}	n_{obs}	σ_b	σ_y	$\sigma_{(b+y)/2}$
1461	2361	561	8	19	1301	0.00054	0.00060	0.00049
G3V	F3V	F3IV				(0.00049)	(0.00042)	(0.00043)
						0.00039	0.00050	0.00035
1835	1594	2488	4	24	1143	0.00792	0.00739	0.00764
G2.5V	G8III	F6V				(0.00074)	(0.00059)	(0.00056)
						0.00790	0.00738	0.00763
							2007 →	[0.0087]
4307	2630	4048	8	17	807	0.00016	0.00038	0.00018
G0V	F2/3V	F8				(0.00057)	(0.00048)	(0.00050)
						...	0.00008	...
6920	6585	6338	8	21	1462	0.00086	0.00083	0.00080
F9IV	F5	F3V				(0.00052)	(0.00032)	(0.00036)
						0.00076	0.00079	0.00075
9562	10009	10116	4	19	888	0.00052	0.00058	0.00050
G1V	F3V	F5V				(0.00095)	(0.00078)	(0.00076)
						...	...	...
9986	8402	10016	11	16	1062	0.00062	0.00075	0.00060
G2V	F0	F5				(0.00053)	(0.00053)	(0.00046)
						0.00047	0.00063	0.00048
10145	9614	13540	8	19	2502	0.00055	0.00045	0.00028
G5V	A0	F5				(0.00043)	(0.00054)	(0.00040)
						0.00044	0.00020	...
10307	8671	8799	8	21	2662	0.00034	0.00028	0.00029
G1V	F7V	F4V				(0.00057)	(0.00035)	(0.00041)
						...	...	...
10476	9780	10697	4	17	691	0.00185	0.00237	0.00204
K1V	F0V	G3Va				(0.00105)	(0.00096)	(0.00095)
						0.00168	0.00226	0.00191
							2007 →	[0.0014]
10700	9061	10453	4	21	700	0.00122	0.00108	0.00107
G8V	F3/5V	F6V				(0.00130)	(0.00142)	(0.00130)
						0.00077	0.00035	0.00051
13043	12382	14128	8	16	1125	0.00027	0.00043	0.00028
G2V	F8	F0				(0.00033)	(0.00037)	(0.00027)
						...	0.00031	0.00015
13421	15115	13683	4	21	996	0.00110	0.00186	0.00145
G0IV	F4IV	F0				(0.00084)	(0.00103)	(0.00089)
						0.00090	0.00169	0.00128
							2007 →	[0.0007]
18256	17918	18404	4	24	1215	0.00197	0.00233	0.00212
F6V	F5III	F5V				(0.00054)	(0.00056)	(0.00051)
						0.00192	0.00229	0.00208
							2007 →	[0.0014]
19373	19845	18768	8	21	2220	0.00052	0.00027	0.00032
F9.5V	K0III	G1V				(0.00027)	(0.00031)	(0.00026)
						0.00046	0.00007	...
20630	21018	21585	4	19	1759	0.00841	0.00774	0.00805
G5V	G2III	G1IV				(0.00102)	(0.00134)	(0.00110)
						0.00838	0.00768	0.00801
30495	31414	30606	4	23	2462	0.00681	0.00591	0.00636
G2.5IV-V	G9III	F8V				(0.00090)	(0.0065)	(0.00073)
						0.00678	0.00589	0.00634

Table 2
(Continued)

HD	HD Comp2	HD Comp3	Tel	$N_{\rm years}$	$n_{\rm obs}$	σ_b	σ_y	$\sigma_{(b+y)/2}$
32147	32306	33256	4	23	1472	0.00170	0.00169	0.00156
K4V	F0V	F5V				(0.00101)	(0.00114)	(0.00105)
						0.00153	0.00147	0.00136
35296	38558	39587	4	24	16555	0.00324	0.00277	0.00299
F8V	F4III	G0V				(0.00081)	(0.00073)	(0.00073)
						0.00318	0.00271	0.00294
							2007 →	[0.0045]
38858	38273	38089	8	20	2225	0.00030	0.00041	0.00032
G2V	F2	F5V				(0.00034)	(0.00030)	(0.00023)
						0.00011	0.00033	0.00023
39587	38558	37147	4	24	1645	0.00480	0.00438	0.00455
G0V	F4III	F0V				(0.00079)	(0.00072)	(0.00072)
						0.00476	0.00435	0.00452
							2007 →	[0.0062]
42618	43338	42548	11	16	2359	0.00062	0.00040	0.00038
G4V	F0	F0				(0.00059)	(0.00076)	(0.00026)
						0.00044	...	0.00029
42807	42548	44497	8	18	1796	0.00760	0.00663	0.00711
G5V	F0	F1V				(0.00029)	(0.00047)	(0.00032)
						0.00760	0.00662	0.00710
43587	43856	43823	4	17	1415	0.00118	0.00101	0.00108
G0V	F6V	F2V				(0.00086)	(0.00094)	(0.00084)
						0.00099	0.00073	0.00088
50692	48548	50554	4	16	1151	0.00168	0.00217	0.00190
G0V	A3/4	F8V:				(0.00050)	(0.00058)	(0.00057)
						0.00163	0.00212	0.00184
52711	54777	53744	4	17	1250	0.00086	0.00119	0.00097
G0V	F2IV	B9IV				(0.00090)	(0.00053)	(0.00065)
						0.00054	0.00111	0.00082
55575	56245	55576	4	17	1433	0.00065	0.00099	0.00076
F9V	K0III	K0III				(0.00120)	(0.00119)	(0.00113)
						...	0.00049	...
72905	75486	73108	4	23	2131	0.01252	0.01130	0.01190
G0.5V	F0IV	K1+III				(0.00077)	(0.00091)	(0.00075)
						0.01251	0.01128	0.01189
75332	73596	77408	4	24	1605	0.00480	0.00462	0.00468
F7V	F5III	F6V				(0.00117)	(0.00095)	(0.00102)
						0.00472	0.00456	0.00462
							2007 →	[0.0057]
76151	74688	76735	4	24	1875	0.00155	0.00151	0.00152
G2V	F5V	F3V				(0.00098)	(0.00105)	(0.00098)
						0.00137	0.00130	0.00134
78366	78234	77408	4	24	1875	0.00411	0.00407	0.00406
G0IV-V	F3V	F6V				(0.00069)	(0.00056)	(0.00057)
						0.00407	0.00405	0.00404
81809	81464	81997	4	19	1482	0.00144	0.00150	0.00144
G1.5IV-V	F3/5V	F5.5IV-V				(0.00097)	(0.00120)	(0.00094)
						0.00125	0.00122	0.00126
							2007 →	[0.0006]
82885	83525	83951	4	24	1907	0.00208	0.00266	0.00235
G8Va	F5	F23V				(0.00039)	(0.00066)	(0.00035)
						0.00205	0.00261	0.00233
							2007 →	[0.0050]

Table 2
(Continued)

HD	HD Comp2	HD Comp3	Tel	$N_{\rm years}$	$n_{\rm obs}$	σ_b	σ_y	$\sigma_{(b+y)/2}$
86728	87822	85016	8	18	1956	0.00047	0.00035	0.00023
G4V	F4V	A6V				(0.00029)	(0.00032)	(0.00024)
						0.00040	0.00023	0.00005
88986	88476	89557	8	15	1539	0.00025	0.00036	0.00027
G2V	G8III	G8III				(0.00029)	(0.00036)	(0.00029)
						0.00004	0.00020	0.00012
89269	91060	88923	11	14	2912	0.00081	0.00049	0.00058
G6V	F3V	F0V				(0.00037)	(0.00034)	(0.00020)
						0.00075	0.00041	0.00055
90508	90807	89652	4	20	2058	0.00082	0.00105	0.00089
G0V	G8III	G0V:				(0.00081)	(0.00126)	(0.00101)
						0.00054	0.00050	0.00050
95128	92370	94669	4	20	2334	0.00092	0.00094	0.00092
G1V	F2V	K2III				(0.00109)	(0.00104)	(0.00105)
						0.00045	0.00056	0.00050
97334	101501	99373	4	24	1723	0.00926	0.00792	0.00858
G1V	G8V	F5.5IV-V				(0.00552)	(0.00487)	(0.00517)
						0.00839	0.00713	0.00776
101364	99760	101193	8	9	1859	0.00020	0.00036	0.00021
G0V	F2	F5				(0.00017)	(0.00023)	(0.00016)
						0.00008	0.00029	0.00010
101501	101606	99373	4	24	1741	0.00614	0.00532	0.00573
G8V	F5V	F5.5IV-V				(0.00132)	(0.00181)	(0.00154)
						0.00607	0.00516	0.00562
109358	108464	109615	4	18	1730	0.00089	0.00110	0.00094
G0V	G7III+A7III	A0V				(0.00111)	(0.00151)	(0.00128)
						0.00037	0.00019	0.00013
115043	113253	114446	8	20	1803	0.00580	0.00479	0.00529
G1Va	K0III	F8V				(0.00096)	(0.00081)	(0.00085)
						0.00576	0.00475	0.00525
115383	117176	112503	4	20	1598	0.00511	0.00458	0.00484
G0IV	G5V	F7IV				(0.00089)	(0.00116)	(0.00098)
						0.00507	0.00450	0.00479
							2007 →	[0.0048]
115617	114946	113415	4	16	1080	0.00056	0.00050	0.00050
G7V	G9IV	F8.5V				(0.00096)	(0.00095)	(0.00089)
						...	...	...
117176	117304	112503	4	20	1579	0.00124	0.00192	0.00156
G5V	K0III	F7IV				(0.00123)	(0.00173)	(0.00144)
						0.00086	0.00146	0.00116
120066	120317	122797	8	15	1299	0.00043	0.00042	0.00040
G0V	F2IV	F3V				(0.00039)	(0.00037)	(0.00035)
						0.00029	0.00030	0.00028
120136	121560	120601	4	18	1520	0.00208	0.00266	0.00235
F7IV-V	F7V	F3III				(0.00039)	(0.00066)	(0.00035)
						0.00205	0.00261	0.00233
							2007 →	[0.0030]
126053	122797	124115	4	24	1942	0.00136	0.00159	0.00143
G1.5V	F3V	F8V				(0.00080)	(0.0087)	(0.00082)
						0.00122	0.00145	0.00129
140538	138290	141004	4	24	1964	0.00111	0.00099	0.00103
G2.5V	F2Vs	G0IV-V				(0.00071)	(0.00071)	(0.00057)
						0.00096	0.00083	0.00092

Table 2
(Continued)

HD	HD Comp2	HD Comp3	Tel	N_{years}	n_{obs}	σ_b	σ_y	$\sigma_{(b+y)/2}$
141004	142267	140538	4	20	1115	0.00084	0.00075	0.00070
G0-V	G0V	G5V				(0.00108)	(0.00101)	(0.00102)
						0.00027	0.00011	...
143761	140716	144359	4	17	1552	0.00154	0.00247	0.00198
G0+Va	K0III	A0II-III				(0.00087)	(0.0083)	(0.00078)
						0.00139	0.00239	0.00189
							2007 →	[0.0009]
146233	143841	144892	8	17	2918	0.00054	0.00037)	0.00040
G2Va	F3V	F7V				(0.00030)	(0.00028)	(0.00025)
						0.00048	0.00028	0.00033
149661	151783	151900	4	24	1226	0.00579	0.00479	0.00527
K0V	F0	F3V				(0.00086)	(0.00077)	(0.00071)
						0.00575	0.00476	0.00524
							2007 →	[0.0066]
152391	150557	150050	4	24	1039	0.01385	0.01194	0.01289
G8.5V	F2IV+	K2III				(0.00095)	(0.00116)	(0.00099)
						0.01383	0.01191	0.01287
							2007 →	[0.0138]
154417	155646	156539	4	20	1013	0.00587	0.00520	0.00553
F9V	F6IV	F3V				(0.00063)	(0.00090)	(0.00070)
						0.00585	0.00516	0.00550
157214	154888	159733	8	16	1290	0.00052	0.00056	0.00042
G0V	A0	F0				(0.00057)	(0.00046)	(0.00047)
						0.00030	0.00043	0.00022
159222	159733	156757	8	19	1549	0.00069	0.00038	0.00046
G1V	F0n	A5				(0.00052)	(0.00033)	(0.00039)
						0.00056	0.00027	0.00034
160346	158736	158737	4	17	714	0.00155	0.00106	0.00128
K2.5V	F8	F0				(0.00056)	(0.00075)	(0.00062)
						0.00149	0.00089	0.00119
							2007 →	[...]
168009	166409	166955	8	20	2586	0.00028	0.00032	0.00025
G1V	F7IV	G8III				(0.00049)	(0.00052)	(0.00050)
						...	...	...
181655	180915	181656	8	19	1327	0.00076	0.00036	0.00041
G5V	A2	F5				(0.00040)	(0.00049)	(0.00039)
						0.00069	...	0.00027
185144	179729	194031	4	15	936	0.00126	0.00099	0.00110
G9V	F7V	F0				(0.00077)	(0.00055)	(0.00057)
						0.00111	0.00088	0.00100
							2007 →	[<0.0019]
186408	186427	184960	8	13	1673	0.00046	0.00036	0.00040
G3V	G4V	F8V				(0.00041)	(0.00044)	(0.00040)
						0.00033	0.00013	0.00024
186427	186408	184960	8	13	1673	0.00047	0.00042	0.00044
G3V	G1.5V	F8V				(0.00040)	(0.00036)	(0.00036)
						0.00035	0.00031	0.00033
187691	187923	191104	4	16	938	0.00119	0.00167	0.00134
F8V	G0V	F3V				(0.00048)	(0.00037)	(0.00039)
						0.00112	0.00164	0.00130
187923	187691	185206	4	18	994	0.00103	0.00213	0.00151
G0V	F8V	F0				(0.00115)	(0.00119)	(0.00103)
						0.00061	0.00195	0.00130

Table 2
(Continued)

HD	HD Comp2	HD Comp3	Tel	$N_{\rm years}$	$n_{\rm obs}$	σ_b	σ_y	$\sigma_{(b+y)/2}$
190406	189410	190151	4	20	1286	0.00168	0.00261	0.00211
G0V	F1Vn	G0				(0.00077)	(0.00083)	(0.00077)
						0.00158	0.00254	0.00202
197076	198135	198346	4	17	913	0.00066	0.00144	0.00095
G1V	F8	F0				(0.00083)	(0.00094)	(0.00080)
						0.00020	0.00126	0.00074
201091	200077	201154	8	15	1007	0.00291	0.00241	0.00264
K5V	F8V	F5				(0.00045)	(0.00042)	0.00037
						0.00289	0.00239	0.00262
							2007 →	[<0.0030]
201092	200077	201154	8	15	1018	0.00266	0.00224	0.00242
K7V	F8V	F5				(0.00046)	(0.00042)	(0.00036)
						0.00264	0.00221	0.00240
							2007 →	[<0.0024]
206860	207652	209166	4	20	1011	0.00647	0.00649	0.00645
G0V	F2IV	F0III				(0.00142)	(0.00122)	(0.00124)
						0.00639	0.00643	0.00639
217014	217783	218079	4	19	1029	0.00098	0.00165	0.00120
G2IV	F5IV	F0				(0.00039)	(0.00083)	(0.00052)
						0.00092	0.00153	0.00112
224930	223486	2233323	4	19	1017	0.00133	0.00217	0.00172
G5Vb	F0IV-V	F3IV				(0.00104)	(0.00115)	(0.00107)
						0.00109	0.00200	0.00153

almost no missing seasons internally, but the sparser S-index data series contain gaps, corresponding either to seasons with no data or to seasons with fewer than six observations that were excluded from our analysis, as mentioned previously.

Figure 4(a) shows the annualized time series for HD 20630, a very active star with log $R'_{\rm HK} = -4.44$; Figure 4(b) shows the active star HD 30495 with log $R'_{\rm HK} = -4.51$; Figure 4(c) shows the solar twin HD 146233 (18 Sco) with log $R'_{\rm HK} = -4.93$; and Figure 4(d) shows the very inactive star HD 4307 with log $R'_{\rm HK} = -5.20$. Photometric variability follows the same strong-to-weak progression. In Figures 4(a) and (b), the program star photometric variability is cleanly exhibited, with the comparison star variability barely noticeable. In Figure 4(c), comparison star variability starts to intrude more insistently, although not to the degree that it dominates; in this particular case, 18 Sco's intrinsic variability is clearly evident owing to a pair of extremely stable comparison stars. In Figure 4(d), the program star and its two comparison stars are all extremely quiescent, and the apparent variation in the S-index between seasons 6–16, relative to its absence from seasons 17–25, illustrates the dramatic improvement in the SSS observations after the camera change in 2008. Similar stackplots for all 72 stars of this study are included in the extended figure as Figures 4.1–4.72, which are arranged in HD number order.

The ability to visually discern patterns of variation in a display like Figure 4 is hampered by the seasonal chopping of the stellar time series, as well as the tendency of young, active stars to vary irregularly. Nevertheless, the pattern among young, active stars to become fainter as their H+K emission increases on the year-to-year timescale and longer is fairly evident, as is the complex, irregular pattern of this variability (e.g., Figures 4(a) and (b)). Among the less active stars, the variability timescale seems to be longer and multiyear trends are smoother. There is some preference for a pattern of direct correlation between photometric and chromospheric H+K emission variations. HD 146233 is a particularly clear example of these behaviors (Figure 4(c)).

Regular, smooth cyclic behavior like the Sun's does not appear to be common among the 72 stars, although several do exhibit it. Figure 5, which is analogous to Figure 2, illustrates this. The relatively short duration of the present time series and, in particular, the brief eight years of the "CCD-2" era of high-quality SSS observations perhaps render judgment in this matter somewhat premature. As before, the selection was made by subjective inspection, the criterion being the impression of a simple, regular, quasi-sinusoidal activity cycle in the time series, with a single timescale dominating the variation. Unlike the earlier evaluation of the Mount Wilson sample, which appeared to show that Sun-like cycles occur mainly among K-type stars, the present exercise clearly shows that stars very similar to the Sun in $B - V$ color and average activity level do sometimes also display Sun-like activity cycles—the earlier result was presumably a selection effect.

4. Intercomparison of Solar and Stellar Data

We now return to the issue of placing the Sun in its stellar context, which depends on accurate conversions of solar data to the measurement systems used for our stellar observations. The conversion should be, in principle, relatively straightforward for chromospheric emission: because the NSO 1 Å K-index and the Lowell SSS HK-index both measure Ca II emission, any differences should be mostly instrumental, rather than astrophysical, in origin. In contrast, the conversion between TSI and Strömgren *b* and *y* variability forces us to confront head on the issue of relating SSI to TSI on the decadal timescale, as discussed in the introduction to this paper.

Table 3
LOWELL/SSS Spectroscopic Results

Star	Date Range	$N_{n>5}$	Mean S	σ_S	$d(\mathrm{mag})/dS$	SE Slope
Sun	1994–2016	23	0.1717	0.0050	0.0122(1)	0.0114
1461	1997–2016	14	0.1550	0.0046	0.0826	0.0225
1835	1992–2016	19	0.3200	0.0157	−0.3380	0.1130
4307	1997–2016	19	0.1320	0.0023	0.0050	0.0213
6920	1996–2016	16	0.1866	0.0074	0.0263	0.0227
9562	1992–2016	11	0.1336	0.0029	−0.0166	0.0690
9986	2008–2014	4	0.2017	0.0034	...	...
10145	2008–2014	2	0.1709	0.0007	...	...
10307	1994–2016	22	0.1564	0.0046	−0.0512	0.0126
10476	1992–2016	16	0.1803	0.0125	0.0913	0.0436
10700	1994–2016	15	0.1744	0.0042	−0.0280	0.0712
13043	2008–2014	3	0.1559	0.0020	...	...
13421	1993–2016	10	0.1285	0.0040	−0.2190	0.1690
18256	1992–2016	13	0.1737	0.0105	0.1746	0.0503
19373	2006–2016	9	0.1521	0.0005	0.2240	0.1810
20630	1996–2016	20	0.3559	0.0099	−0.5180	0.1430
30495	1996–2016	20	0.2997	0.0102	−0.4843	0.0574
32147	2008–2016	5	0.2655	0.0273	0.0043	0.0359
35296	1992–2016	18	0.3131	0.0094	−0.0522	0.0823
38858	1997–2016	18	0.1783	0.0036	0.0554	0.0119
39587	1992–2016	19	0.3344	0.0093	−0.2661	0.0915
42618	2008–2014	3	0.1649	0.0050	...	...
42807	1997–2016	11	0.3308	0.0210	−0.3120	0.1040
43587	1994–2016	19	0.1580	0.0038	−0.0010	0.1070
50692	2007–2016	9	0.1596	0.0010	1.0350	0.5680
52711	1997–2016	18	0.1613	0.0029	0.2520	0.1220
55575	2009–2016	7	0.1606	0.0006	−0.4230	0.5750
72905	1994–2016	11	0.3670	0.0125	−0.8780	0.2500
75332	1994–2016	10	0.2374	0.0075	−0.2050	0.1420
76151	1994–2016	19	0.2324	0.0122	−0.0958	0.0209
78366	1994–2016	14	0.2346	0.0093	−0.1650	0.1250
81809	1994–2016	21	0.1627	0.0078	−0.0039	0.0489
82885	1993–2016	20	0.2588	0.0194	−0.4359	0.0499
86728	1994–2016	12	0.1418	0.0030	0.0479	0.0770
88986	1998–2016	17	0.1321	0.0024	0.0290	0.0353
89269	2005–2015	6	0.1548	0.0034	0.0623	0.0676
90508	1998–2016	17	0.1487	0.0030	−0.0913	0.0710
95128	2004–2016	12	0.1491	0.0003	0.0900	0.7930
97334	1998–2016	18	0.3177	0.0130	−0.3390	0.1370
101364	2009	1	0.1638	...	...	...
101501	1994–2016	14	0.3219	0.0276	−0.1593	0.0527
109358	2004–2016	12	0.1591	0.0009	−0.4830	0.3220
115043	2009–2016	8	0.2961	0.0060	−0.5280	0.2130
115383	1994–2016	17	0.3059	0.0086	−0.3530	0.1080
115617	2004–2016	10	0.1644	0.0039	−0.0392	0.0343
117176	1998–2016	14	0.1270	0.0028	−0.2780	0.1370
120066	2009–2016	8	0.1401	0.0009	0.2370	0.1260
120136	1998–2016	16	0.1920	0.0034	−0.2770	0.1960
126053	2007–2016	18	0.1681	0.0029	0.3040	0.1010
140538	1997–2016	20	0.2215	0.0149	−0.0555	0.0117
141004	1997–2016	13	0.1602	0.0025	0.1671	0.0813
143761	1997–2016	15	0.1442	0.0029	0.8440	0.4050
146233	1997–2016	20	0.1724	0.0058	0.0342	0.0181
149661	1994–2016	11	0.2725	0.0155	−0.1878	0.0679
152391	2008–2015	7	0.3825	0.0192	0.8360	0.1170
154417	2008–2016	9	0.2863	0.0043	0.0050	0.2750
157214	2007–2016	20	0.1556	0.0023	−0.1014	0.0674
159222	2008–2016	8	0.1774	0.0058	0.0035	0.0290
160346	2008–2010	3	0.2850	0.0182	...	...
168009	1997–2016	19	0.1605	0.0028	0.0246	0.0215
181655	1997–2016	12	0.1653	0.0029	0.0837	0.0341
185144	1994–2016	14	0.2139	0.0127	0.0698	0.0155
186408	1996–2016	21	0.1484	0.0018	0.1946	0.0539
186427	1996–2016	21	0.1536	0.0020	−0.2040	0.1030

Table 3
(Continued)

Star	Date Range	$N_{n>5}$	Mean S	σ_S	$d(\text{mag})/dS$	SE Slope
187691	1996–2016	10	0.1407	0.0034	0.5500	0.5430
187923	1997–2016	19	0.1518	0.0022	−0.0707	0.0956
190406	1997–2016	19	0.1989	0.0070	−0.0664	0.0724
197076	1998–2016	16	0.1752	0.0048	−0.0549	0.0555
201091	1992–2016	16	0.6199	0.0554	0.0183	0.0122
201092	1992–2016	16	0.7696	0.0950	0.0083	0.0037
206860	1999–2016	10	0.3217	0.0109	−0.5940	0.1340
217014	1996–2016	13	0.1470	0.0013	−0.1960	0.2920
224930	2005–2016	12	0.1762	0.0024	−0.3960	0.1830

Note. (1) Regression of TSI (in magnitude units) on S-index for the Sun.

Table 4
Description of Seasonal Data File

Column	Description
1	Henry Draper Catalog number
2	APT midseason epoch
3	Number of photometric observations
4	Seasonal $(b + y)/2$ tri-mean, prog. star–mean comp. star (1)
5	95% confidence interval, upper range (brighter)
6	95% confidence interval, lower range (fainter)
7	Seasonal $(b + y)/2$ tri-mean, comp2–comp3 (1)
8	95% confidence interval, upper range (brighter)
9	95% confidence interval, lower range (fainter)
10	SSS mid-season epoch
11	Number of S-index observations
12	Seasonal median S-index
13	95% confidence interval, upper range
14	95% confidence interval, lower range
15	Seasonal median log R'_{HK}
16	Season number beginning with 1992–1993

Note. (1) Relative to the grand mean of all of the photometric observations.

(This table is available in its entirety in machine-readable form.)

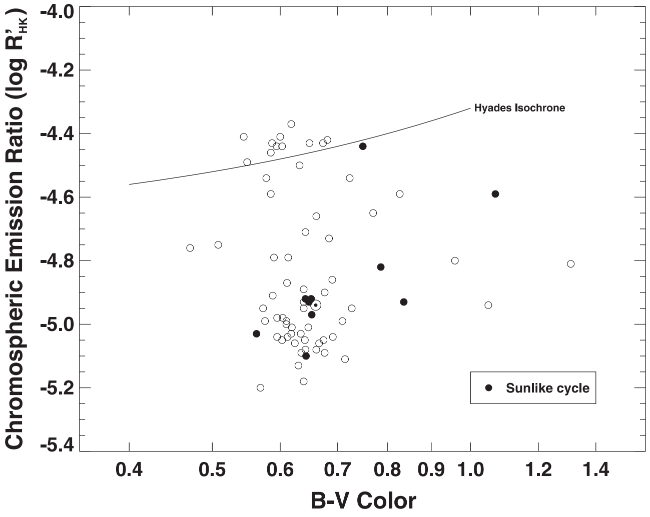

Figure 5. The 72 stars of the present sample, displayed as a color–activity diagram. The Sun's location is also indicated. Stars with simple Sun-like activity cycles are plotted with filled symbols; the 10 stars so selected are HD 9986, HD 10476, HD 81809, HD 89269, HD 146233, HD 152391, HD 185144, HD 186408, HD 187691, and HD 201091.

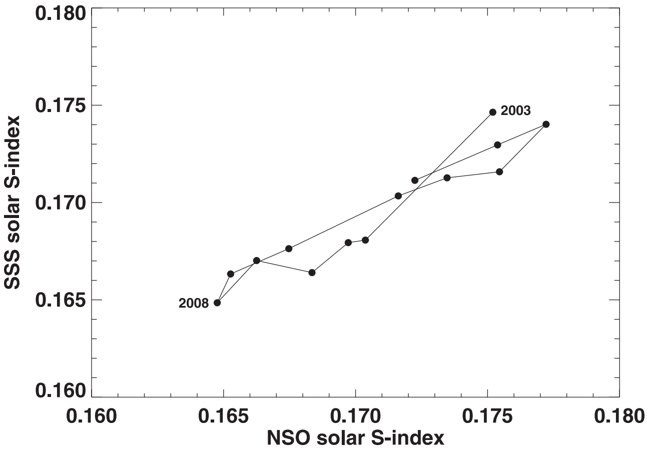

Figure 6. Scatter plot of the NSO solar S-index vs. the SSS solar S-index plotted for 2003–2016, with the annual points linked to emphasize the temporal trajectory the relationship follows. The SSS data divide into two epochs: 2003–2008 (the original TeK CCD camera) and 2008–2016 (the new Andor CCD camera). The label "2008" marks this division.

4.1. NSO K-index, SSS HK-index, and the MWO S-index

A detailed study of the NSO 1 Å K-index (K), the Lowell Observatory SSS solar HK-index, and their conversion to the instrumental Mount Wilson Observatory S-index (S) has recently been published by Egeland et al. (2017b). We adopt their relation

$$S = 1.708{*}K + 0.024 \tag{2}$$

for converting the NSO K-index to the Mount Wilson S-index, with a digit added to the coefficients to enforce comparable precision among the quantities.

In Figure 6, we show annual averages for 2003–2016 for the (converted) NSO S-index versus the SSS solar S-index plotted as a scatter plot with the annual points linked to emphasize the temporal trajectory that the relationship follows. The correlation coefficient is 0.954, which is (not unexpectedly) highly significant. Closer examination shows that the measured amplitude of the solar cycle is greater for the NSO data than the SSS data; furthermore, a best-fit linear regression (not shown) has a slope of 0.72 and a y-intercept of 0.046, so the correspondence is clearly not perfect. However, because we ultimately use SSS measurements for both the Sun and stars, these discrepancies should be unimportant.

4.2. Photometry and TSI/SSI

We examined the relationship between TSI and Strömgren b and y variability on the decadal timescale by analyzing the

SORCE TSI and SSI time series over the entire duration of the *SORCE* mission, from early 2003 through mid-2017. This 14+ year interval spans an entire solar cycle, from the initial decline of cycle 23 in 2003 through the initial decline of the current cycle 24 in 2015–2017, and thereby offers a longer perspective on the behavior of both the Sun and the *SORCE* instruments compared to the shorter 2003–2007 interval considered previously (Harder et al. 2009; Haigh et al. 2010).

We downloaded the *SORCE* SSI and TSI data used in this paper in 2017 mid-August from the *SORCE* Web site (http://lasp.colorado.edu/home/sorce/data/)—according to the release notes, we downloaded Version 23 of the *SORCE*/SIM data and Version 17 of *SORCE*/TIM. From the *SORCE*/SIM data, we produced and analyzed three time series, synthetic Strömgren b, ("SIM-b"), synthetic Strömgren y ("SIM-y"), and an integrated time series spanning 240–1598 nm ("iSSI"), each derived by integrating appropriate parts of the SSI measurements using a simple boxcar procedure. We tapered the SIM-b and SIM-y inputs by the response functions for the Strömgren b and y pass bands, respectively, normalized to unity at peak response. The resulting time series are shown in Figure 7.

As noted in the *SORCE* SIM Release Notes documents, iSSI captures about 89% of the TSI—most of the missing flux is in the infrared. Until mid-2011, the SIM SSI measurements also included the infrared spectrum from 1598 to 2412 nm, accounting for an additional 8% of the TSI flux. Most of the few percent still missing is in the infrared beyond 2400 nm. We computed a version of iSSI spanning 240–2412 nm for 2003–2011, and simply note that, except for an offset, it tracks the 240–1598 nm version extremely well.

Visual comparison of Figures 1 and 7 shows that iSSI tracks TSI well from 2003 through 2015. Figure 3 of the Version 23 Release Notes shows a time series very similar to our iSSI (or perhaps identical—the caption for Figure 3 of the Release Notes states that the time series shown in that figure extends to 1630 nm, but elsewhere the Release Notes text indicates 1600 nm). The visual correspondence between that time series and ours appears to be virtually perfect.

In comparison, both SIM-b and SIM-y track TSI less well.

These patterns are also seen in annual averages. Analogous to Figure 6, in Figure 8 we show TSI versus the annual averages for iSSI, SIM-b, and SIM-y, all plotted as scatter plots with the annual points linked to emphasize the temporal trajectories each relationship follows. For comparison, we also show the corresponding plot for TSI and the NSO K-index.

Computing standard deviations for the annualized quantities and converting to stellar magnitude units, we find

$$(\sigma_b, \sigma_y, \sigma_{(b+y)/2}, \sigma_{\mathrm{TSI}}) = (0.00040, 0.00055, 0.00047, 0.00025) \tag{3}$$

as our result from the direct use of the *SORCE* solar time series, the first three numbers corresponding directly to our measurements of the stellar photometric brightness variability listed in Table 2. Figure 9 is a stackplot for the solar data, analogous to the stellar stackplots of Figure 4.

There are, however, further considerations. We began analyzing *SORCE* data in 2015, downloading the previous Version 22 of the *SORCE*/SIM data on several occasions over 18 months, the last being in late 2017 April, just before Release 23 became available. The differences between the two versions on the year-to-year timescale of concern here are dramatic, comparable in amplitude to the year-to-year features seen in the present Version 23 time series shown in Figure 7. This fact raises an important question: is the year-to-year structure seen in the SIM-b and SIM-y time series in fact solar in origin, considering that comparable differences are evident between Versions 22 and 23, which presumably have been deemed instrumental?

We have discussed these concerns with the *SORCE* Program Scientist (J. Harder 2017, private communication), who has emphasized that a series of spacecraft problems, starting in 2007 and compounding in 2011, have made it increasingly difficult to characterize the stability of SIM and calibrate its data. The bottom line of these discussions is that the *SORCE* team strongly believes that the most reliable SIM data are those prior to 2011.

In view of these uncertainties, we have revived the indirect approach of our earlier paper (R98), which related small changes in TSI to Strömgren b and y variability by a simple scaling. To first order, a fractional change in bolometric flux is related to a $(b + y)/2$ magnitude difference by

$$\triangle\left[\frac{b+y}{2}\right](\mathrm{mag}) \cong \left(\frac{1.25}{\ln 10}\right)(c_b + c_y)\frac{\triangle F_{\mathrm{bol}}}{F_{\mathrm{bol}}}, \tag{4}$$

where c_b is the (assumed constant) ratio of a fractional change in the Strömgren b flux to a fractional change in the bolometric flux, and similarly for c_y. In R98, we estimated

$$\left(\frac{1.25}{\ln 10}\right)(c_b + c_y) \cong 1.34 \tag{5}$$

from a simple blackbody argument and 1.39 from *SoHO*/VIRGO measurements; we then adapted 1.39 as our conversion factor going forward.

The solar outburst energy concept (Woods et al. 2015) offers a new approach for this procedure. The growth and decay of a solar active region, modulated by solar rotation, produces a distinctive decaying signature in TSI with a timescale of four to six months. In late 2007 and early 2008, this signature was particularly clear because the Sun had only one to three active regions, concentrated on a single hemisphere. Time series for that period are presented in Figure 10. There are two outbursts; the first, beginning at about 2007.95, is seen for four rotations in TSI, after which it is overtaken by the second, which starts at about 2008.24 and persists for perhaps as many as seven rotations. In both outbursts, the first rotation is marked by the superposition of a narrow, negative-going spike in irradiance, produced by the disk-center passage of sunspots, more or less centered on the broader, positive-going facular irradiance peak. In both outbursts, the sunspots have disappeared by the second rotation, leaving only the facular peak.

The outburst signature is, unfortunately, considerably less evident in SSI-b and SSI-y than in TSI, probably owing to the lower precision of these data—the signal is simply overwhelmed by noise. There is also some evidence in Figure 10 of secular drift in these two time series. Not surprisingly, therefore, the extracted value for the conversion factor was somewhat sensitive to the duration selected for an outburst. For example, for the outburst that began at about 2008.24, we used regressions of SIM-b and SIM-y on TSI to extract a value of 1.37 for the conversion factor when four rotations were analyzed, and 1.28 when seven were included. Altogether, analyses of seven outburst periods between 2006 and 2015 yielded a mean value of 1.18 ± 0.40. Although our use of regression analysis presumably minimized the effect of random noise, any baseline drift would, of course, still affect the result, and some residual drift seems to be present in the SIM-b and SIM-y time series. However, the correlation between SIM-b

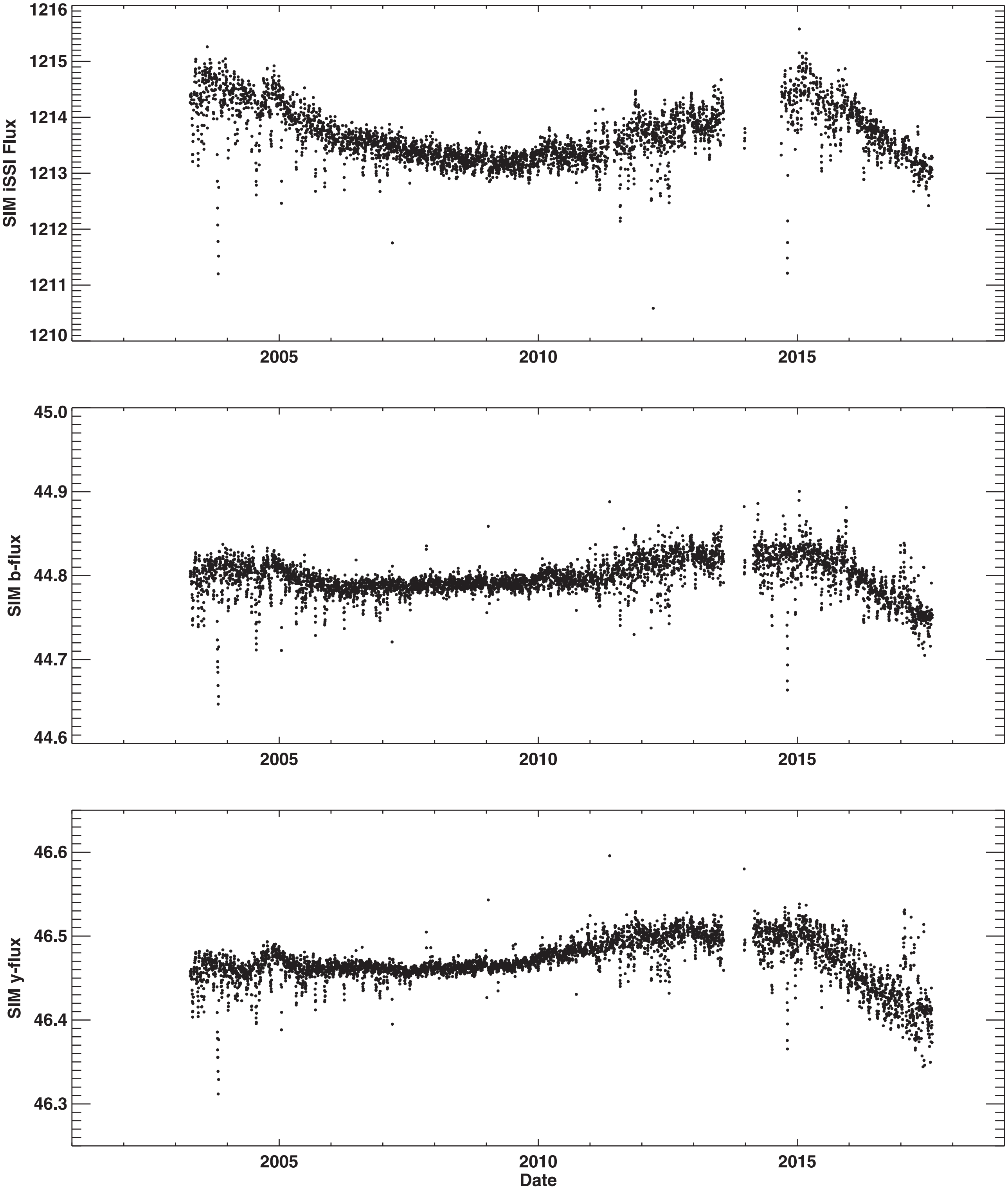

Figure 7. *SORCE*/SIM time series: integrated SIM/SSI (iSSI; top panel), synthetic SIM Strömgren *b* (SIM-*b*; center panel) and synthetic Strömgren *y* (SIM-*y*; lower panel), all in units of Wm^{-2}.

and SIM-*y* variations, on the one hand, and TSI variations, on the other, was invariably found to be positive.

In contrast with entire active region outbursts, it was easy to identify times when the sunspot signature alone was prominent in all three time series—the Halloween events of 2003 October–November, for example. Eleven of these events yielded a value of 1.58 ± 0.31 for the conversion factor. However, because it is the balance between the bright facular component and the dark sunspot component that is of interest when considering solar variability on the decadal timescale, this value, which reflects predominantly sunspot-driven variability, may not include some pertinent physics if the time-integrated radiative properties of sunspots and faculae are not the same.

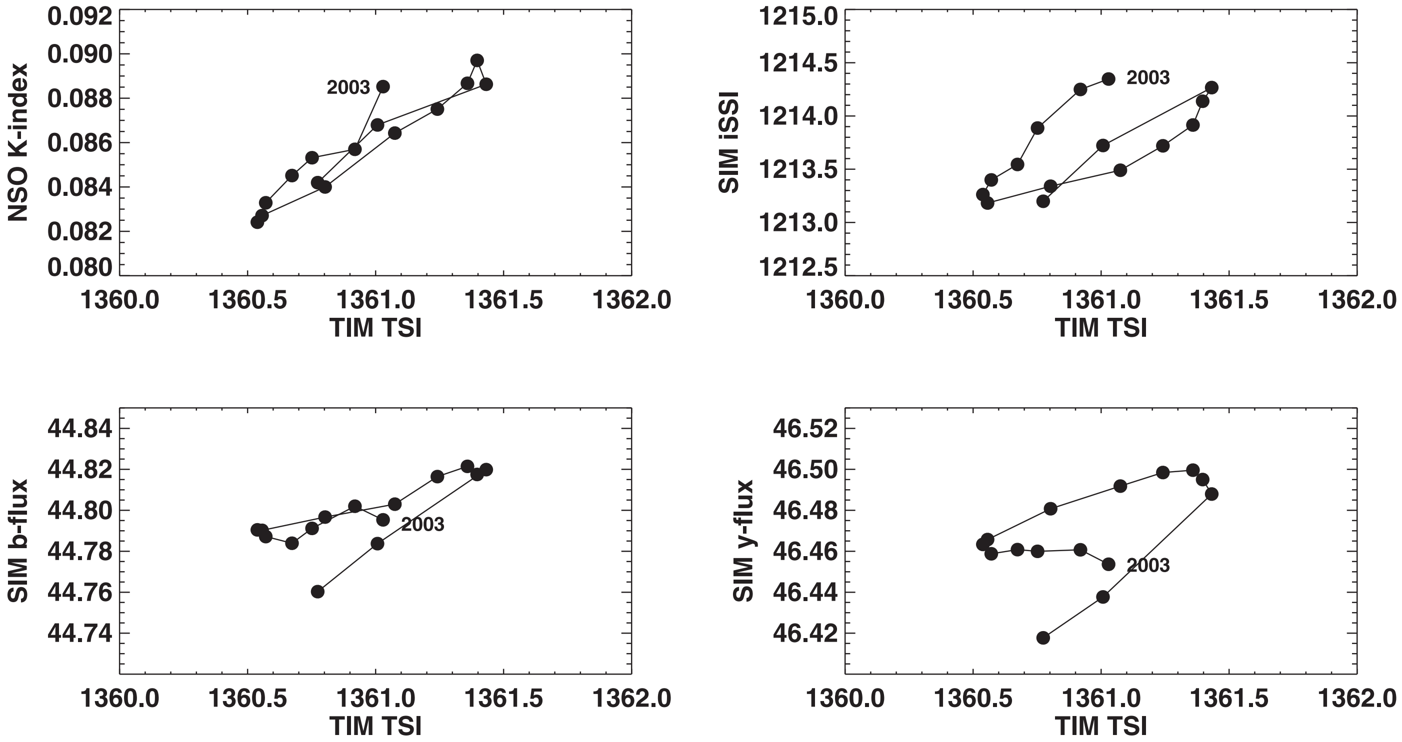

Figure 8. Scatter plots of TSI vs. NSO K-index, iSSI, SIM-*b*, and SIM-*y*, all plotted for 2003–2017 with the annual points linked to emphasize the temporal trajectories each relationship follows.

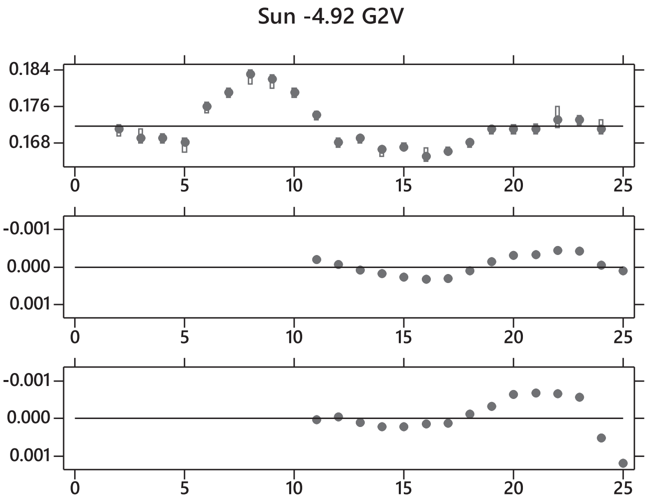

Figure 9. Stackplot of SSS Ca II H+K S-index, *SORCE*/TIM TSI, and synthetic *SORCE*/SIM $(b + y)/2$ seasonal median values for consecutively numbered seasons 1992–1993 to 2016 for the Sun. The upper panel shows the median Lowell SSS S-index (filled circles) and 95% confidence intervals (rectangular boxes). The center panel shows *SORCE*/TIM TSI, converted to stellar magnitude units, and the bottom panel shows the *SORCE*/SIM synthetic $(b + y)/2$, also in magnitude units. The confidence intervals in the lower two panels are barely visible behind the seasonal symbols.

From the results from the direct use of the *SORCE* solar time series, for 2003–2017, presented at the beginning of this subsection (Equation (3)), the value for the conversion factor is

$$\left(\frac{2.5}{\ln 10}\right)\left(\frac{\sigma_{(b+y)/2}}{\sigma_{\mathrm{TSI}}}\right) \cong 2.05. \tag{6}$$

Finally, we simply performed the regression of annually averaged $(\text{SIM-}b + \text{SIM-}y)/2$ on TSI from 2003–2017, obtaining a value of 1.40 for the conversion factor.

Table 5 collects these results.

In summary, the value of 1.39 that we used in 1998 and 2007 for the conversion factor is within the standard error of the value of 1.55 ± 0.37 that we now derive from the *SORCE* data. We note that Sun photometer measurements for 2002–2012 from *SOHO*/VIRGO show that the solar cycle amplitude in the 500 nm band is 1.6× the amplitude in TSI (Wehrli et al. 2013), in good agreement with our present result from the *SORCE* data.

On the outburst timescale, there seems to be little doubt that Strömgren *b* and *y* vary directly with TSI, consistent with the results of Woods et al. (2015). With the further presumption that the solar cycle is the superposition of many individual active region outbursts, we conclude that Strömgren *b* and *y* most likely also vary directly with TSI on the timescale of the solar cycle, as we had assumed in our previous papers.

5. Patterns of Variation for the Sun and Sun-like Stars: Discussion

5.1. Chromospheric Activity Versus Chromospheric Emission Variation

Figure 11(a) shows the relationship between the mean chromospheric Ca II H+K activity (column 4 of Table 3, transformed to R'_{HK} units using the $B - V$ colors from Table 1 in the prescription of Noyes et al. 1984) and chromospheric emission variability (column 5, similarly transformed), along with the best-fit power law, which has a slope of 1.19. The filled symbols are stars from the present sample, whereas the open symbols are the stars from L07. The star HD 101364,

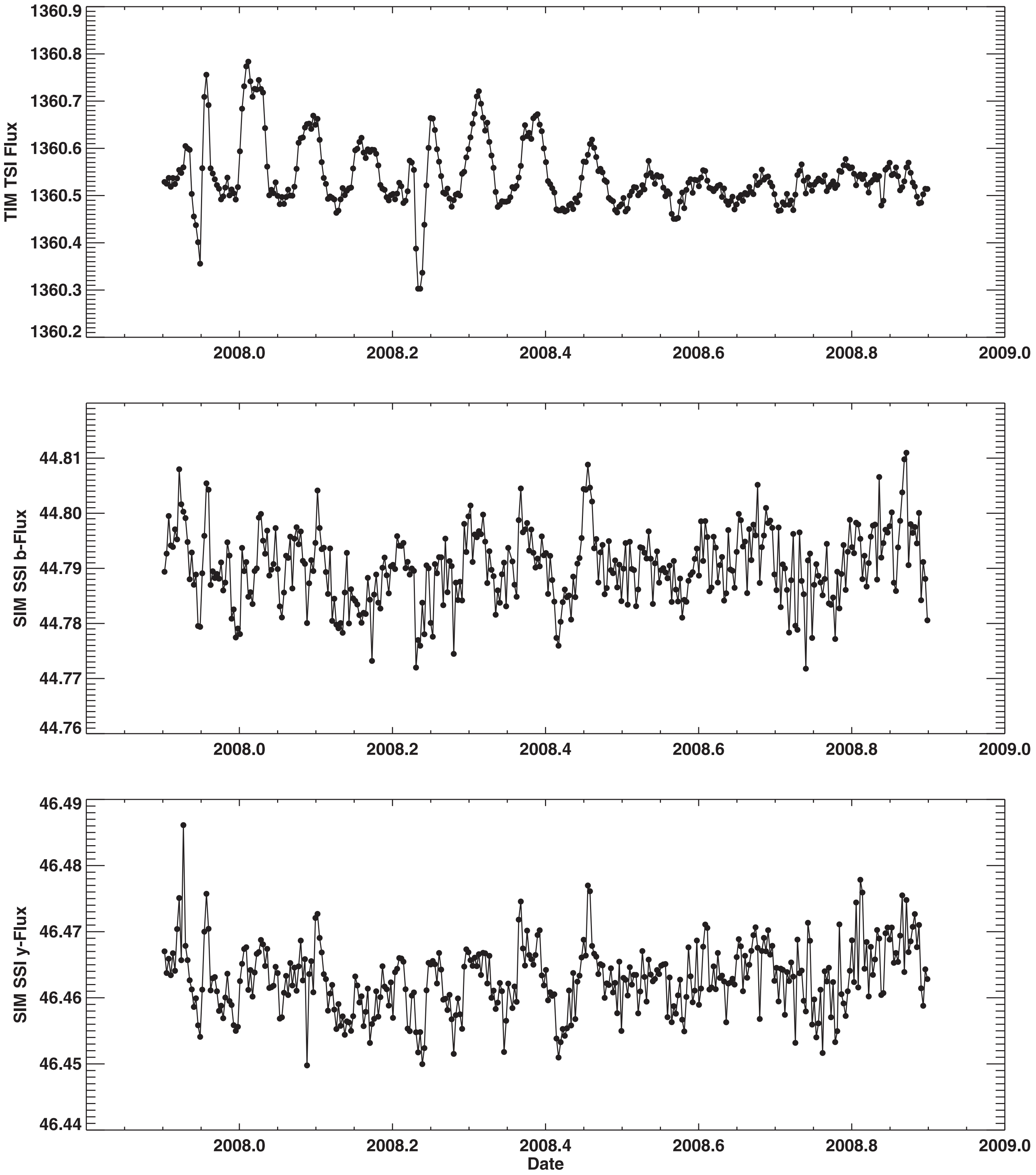

Figure 10. Time series plots of two consecutive solar outburst intervals in late 2007 through 2008: TSI (upper panel), SIM-*b* (center panel), and SIM-*y* (lower panel).

which had only a single acceptable SSS observing season, has been omitted. The symbols for the 18 stars in common are connected by dotted lines. Because the distributions for the two samples look similar, we used both to determine the power law. The Sun is also plotted twice, with the 2017 point labeled. Its trajectory down and to the left between 2007 and 2017 reflects both the comparatively weak Cycle 24 that is now concluding and the recent recalibration of the Sun's S-index to a somewhat lower value (Egeland et al. 2017b). Clearly, there does not appear to be anything unusual about the Sun's location within its stellar context, although is does appear to lie somewhat above the trend line.

Table 5
Summary of Synthetic $(b + y)/2$ vs. *SORCE* TSI Analyses

Analysis Method	Derived Conversion Factor
Direct analysis of *SORCE* time series	2.05
Direct regression of annualized SIM data	1.40
Outburst analysis of eight active regions	1.18
Analysis of 11 sunspot group transits	1.58
Mean	1.55 ± 0.37

The scattering of stars in the lower-left corner of Figure 11(a) could be a result of the tendency of logarithmic units to exaggerate small numbers. In particular, they are not, for the most part, stars that were observed for only a few seasons, a circumstance that could potentially undersample the total range of year-to-year variability. The referee, however, also noticed something that had escaped our attention: the low-variability outliers are, as a group, bluer than the relatively inactive stars with larger variation above them in the diagram. The difference may be marginally significant. The eight outliers with log (rms R'_{HK}) variation less than -6.7 have an average $B - V$ color of 0.62 ± 0.04, and the 42 relatively inactive stars with log (R'_{HK}) activity less than -4.9 (including the eight outliers) have an average color of 0.67 ± 0.13, with a median of 0.64—a bit redder than the outliers alone. The 42 star sample is, however, also biased by the presence of several red stars within it, none of which is an outlier. It is well-known that hotter and more massive main-sequence stars tend to be less active and less variable, a fact that could account for these outliers if the color difference is real, and which may reflect the preferential operation of a shallow dynamo among these stars (Metcalfe et al. 2016; Montet et al. 2017).

An alternative presentation of the data using linear axes is shown as Figure 11(b). The dashed line is the transformed power law, and the dotted line is the best-fit linear regression. The transformed power law is, of course, mathematically constrained to pass through the origin, but the fact that the linear regression also passes near the origin suggests that chromospheric activity and its year-to-year variation both vanish more or less simultaneously.

Figure 11(b), however, also shows quite clearly a floor for chromospheric activity at about $R'_{\mathrm{HK}} \sim 0.5 \times 10^{-5}$ (log $R'_{\mathrm{HK}} \sim -5.3$). This implies that R'_{HK} includes a non-varying component that does not arise from magnetic active regions, i.e., the "basal" chromosphere discussed previously.

5.2. Chromospheric Activity Versus Photometric Brightness Variation

Analogously to Figure 11(a), Figure 12(a) shows the relationship between the mean chromospheric Ca II H+K activity and net intrinsic photometric $(b + y)/2$ brightness variation (i.e., s_1, the left side of Equation (1)). As before, the filled symbols are stars from the present sample, the open symbols are the stars from L07, and the symbols for the 18 stars in common are connected. We use dotted drop lines to show the correction for comparison star variation—clearly, it seldom matters, especially for the stars of the current sample. Ten stars with a negative net variance (essentially, comparison star variance that exceeds the uncorrected program star variance) are located arbitrarily on the figure at 2×10^{-5} and were excluded from the computation of the best-fit power law. Again, both samples were used to compute the trend line, which has a slope of 1.74, somewhat steeper than the power law that relates chromospheric activity to chromospheric emission variation. The Sun is plotted twice; the point labeled "2007" simply reproduces the value in L07, and the point labeled "2017" was determined by scaling the TSI variation derived in Section 4.2 by 1.55 (Table 5) to convert it to stellar magnitude units.

Like Figure 11(b), Figures 12(b) and (c) present the data using linear axes. The curved dashed line is the transformed power law. The dotted line is a linear fit to the data. Figure 12(c) enlarges the lower-left corner of Figure 12(b) and shows the Sun's location more clearly.

The Sun is clearly below the trendlines. Why? Several possible reasons merit consideration.

(1) We have estimated the net variability of our program stars by deducting contributions from the comparison stars and the instrumentation, i.e., we treat it as a residual (Equation (1)). An underestimation or omission in this procedure would result in overstating the variability of the program stars, particularly on the left side (i.e., low variability) side of the distribution, although the right side of the distribution would remain more or less anchored. If the left side of the distribution were adjusted downward, the trend lines would become steeper and move toward the solar points.

In principle, it is possible to test this possibility by examining the behavior of a large sample of non-varying program stars. If Equation (1) is, indeed, a properly calibrated unbiased estimator, then the values for s_1^2 for a sample of non-variable stars should be distributed around zero, with positive and negative values equally likely. Presumably, non-variable stars would also be low-activity stars, with values for $R'_{\mathrm{HK}} < 10^{-5}$ ($\log R'_{\mathrm{HK}} < -5.0$), perhaps. Inspecting Figure 11(c), there are 28 such stars, counting repeats, but only six of these are dropouts (i.e., stars with negative values for s_1^2). Thus, we probably cannot completely exclude the possibility that our variability metric is biased.

(2) The relationship between TSI and Strömgren b, y variability remains less certain than we would like. For example, if we accept the synthetic *SORCE* SIM-b and SIM-y measurements at face value and use them directly to plot the Sun in Figure 12, the 2017 point (as well as the 2007 point, presumably) would move upward by about 30%—not nearly enough to bring it to the center of the stellar distribution, but a bit closer. Until a precise direct measurement of solar Strömgren b and y variability on the decadal timescale is made, however, we will be forced to continue relying on scaling procedures like the ones used in this paper, with all their associated uncertainty.

(3) As discussed in R98 and in subsequent papers (Knaack et al. 2001; Shapiro et al. 2014), the Sun may appear to vary less in photometric brightness than an ensemble of otherwise strictly "solar twin" stars viewed at random inclinations, simply because we view the Sun only from near its equatorial plane, i.e., at inclinations near $i = 90°$. Although they disagree about the magnitude of the effect, models do agree that the observed photometric variation will tend to decease with increasing inclination, and, therefore, be at or near a minimum for the Sun as we actually observe it. We have not applied a correction for this inclination effect in this paper, in part because it has been only modeled and not measured, and partly because we have no assurance that other stars arrange their activity in the Sun-like

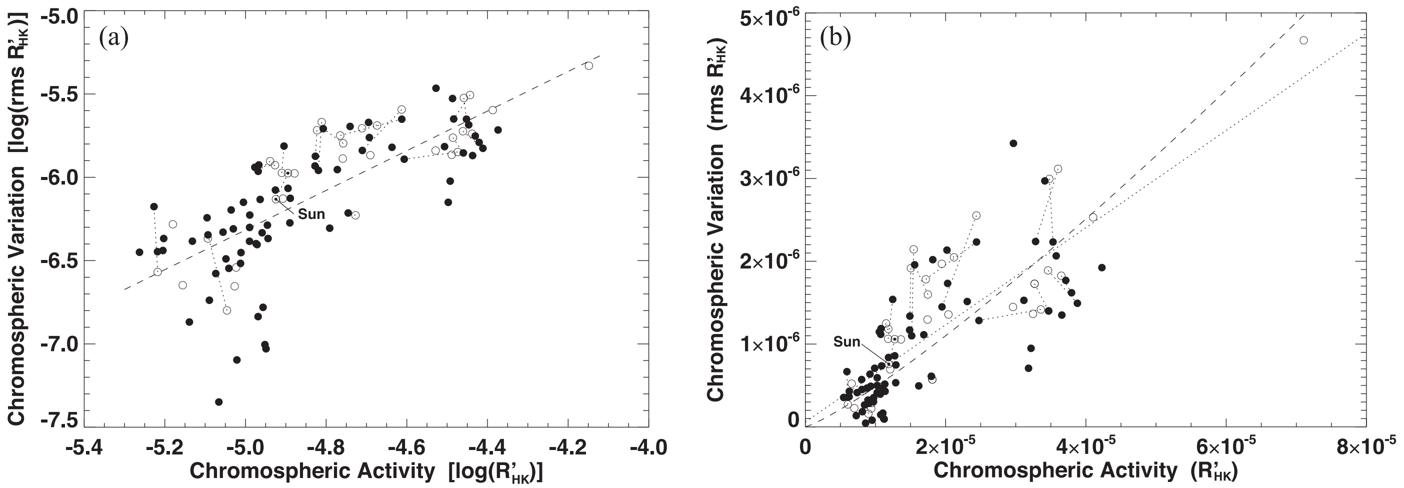

Figure 11. (a) Mean chromospheric Ca H+K activity vs. emission variation (log–log plot). Filled symbols are stars from the present sample, and open symbols are the stars from L07. The symbols for the 18 stars in common are connected by dotted lines. The "Sun" label indicates the present (2017) point. (b) Mean chromospheric Ca H+K activity vs. emission variation (linear scale). The dashed line is the transformed power law, and the dotted line is the best-fit linear regression. The "Sun" label indicates the present (2017) point.

manner of low- to mid-latitude activity belts. In any case, however, it appears that the correction would not be nearly enough to bring the Sun to the center of the stellar distribution.

(4) Metallicity differences, however, are an unlikely explanation. Although metallicity differences probably accentuate the scatter of the distribution (Shapiro et al. 2015; Karoff et al. 2018), they would not create a downward displacement of the Sun relative to the overall distribution unless the Sun were also metal deficient relative to the rest of the stars in the ensemble. To test this possibility, we collected [Fe/H] values for our sample from the (surprisingly heterogeneous) data in SIMBAD; the metallicity of our sample indicated by this exercise is -0.06 ± 0.20 with a median value is -0.01—if anything, the Sun is metal rich relative to the overall sample, although the difference is probably not significant.

(5) Solar chromospheric variability (Figure 11) reflects primarily the properties of solar plages (and, presumably, the underlying faculae), whereas brightness variability (Figure 12) reflects the competitive balance between the radiative properties of both dark sunspots and bright faculae. Accordingly, low brightness variability only tells us that the two components are nearly in balance—it does not, in and of itself, say anything about either of the two components individually. If we interpret the scatter in Figure 12 as indicative of star-to-star differences in this competitive balance, the Sun, albeit an outlier, is not the only one, and the Sun's location below the trend line could be real.

5.3. Chromospheric Emission Variation Versus Photometric Brightness Variation

Finally, we show in Figures 13(a) and (b) the relationship between the chromospheric Ca II H+K emission variation and net intrinsic photometric $(b + y)/2$ brightness variation. As before, the filled symbols are stars from the present sample, the open symbols are the stars from L07, and the symbols for the 18 stars in common are connected. We again use dotted drop lines to show the correction for comparison star variation. Unlike Figure 12, however, we now represent the stars with a negative net intrinsic variance by points below the x-axis (attaching a fictitious negative value to the mathematically imaginary square roots). These stars were, however, excluded from the computation of the best-fit linear regression. Again, both samples were used to compute the trend line. The Sun is plotted twice, as previously.

Two features of these plots are striking:

(1) The points for the 18 stars in common moved around quite a bit between 2007 and 2017 especially in H+K emission. Because the L07 points are based on Mount Wilson H+K measurements and the 2017 points on Lowell SSS measurements, the immediate temptation is to attribute this to instrumental effects. However, closer inspection shows that the offset is not systematic with respect to direction, which would argue against a simple scaling explanation, and the fact that these data are variations precludes a zero-point explanation. Also, the motion of the solar point is comparable to that of the stellar points, and it seems likely that, in the Sun's case, much of the effect has an intrinsic origin: the current solar cycle 24 has been weak, relative to its several predecessors.

(2) Photometric variability appears to vanish at nonzero chromospheric variability. Because Figure 12 shows variations, this cannot be attributed to a non-varying "basal" chromosphere. However, as has been emphasized previously, solar chromospheric variability reflects primarily the properties of solar plages (and, presumably, the underlying faculae), but brightness variability reflects the competitive balance between both dark sunspots and bright faculae. If this interpretation can be generalized validly to stellar variability, then the behavior shown in Figure 13 might not be completely unexpected, i.e., photometric variability (a "difference") might vanish, statistically, at a nonzero value for chromospheric variability (essentially, the facular component, alone, scaled).

5.4. Correlations Between Brightness and Chromospheric Variation

Perhaps the most robust pattern of stellar behavior that we have found over the past 35 years is the division between

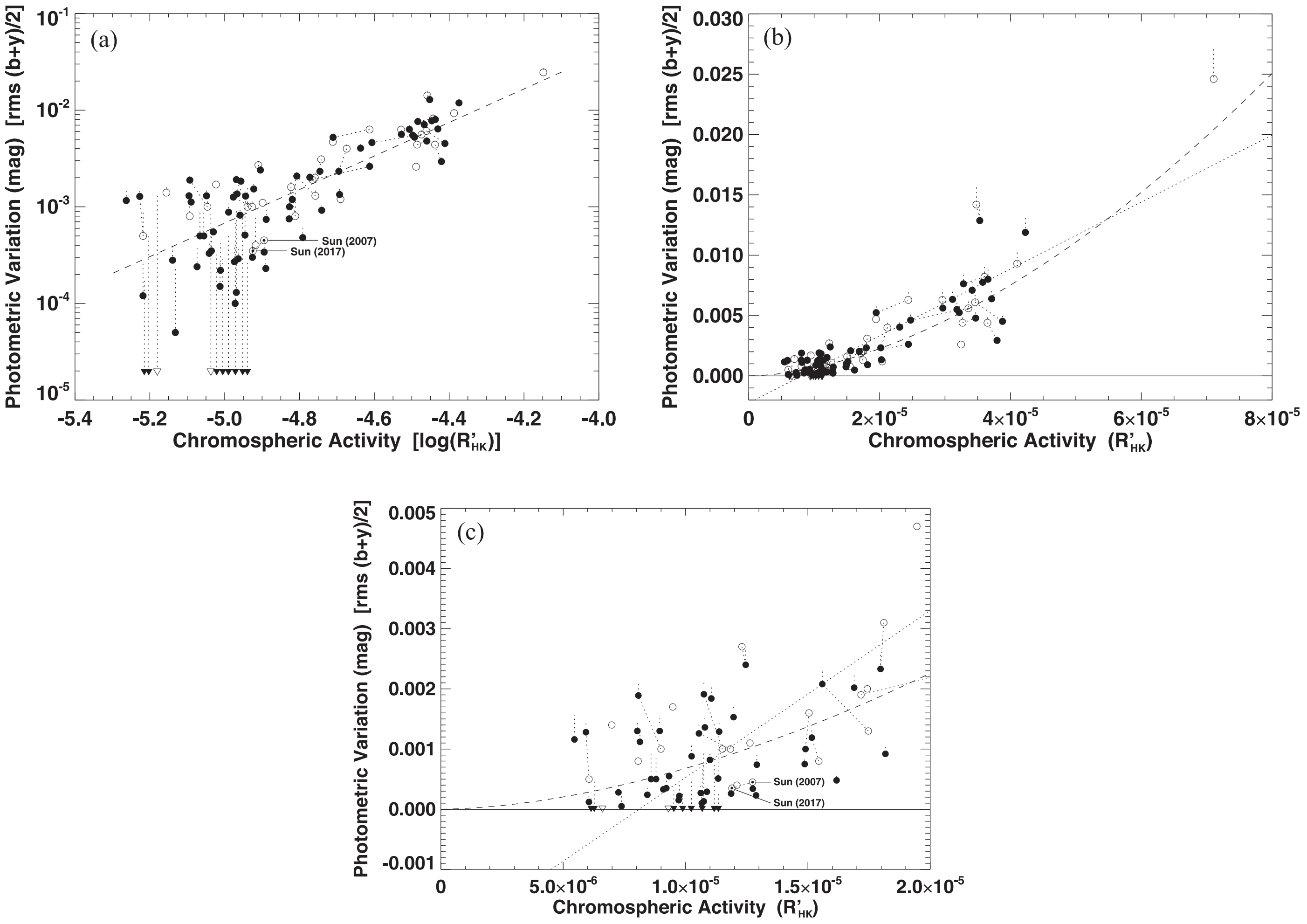

Figure 12. (a) Mean chromospheric Ca H+K activity vs. net intrinsic photometric $(b + y)/2$ brightness variation (log–log plot). Filled symbols are stars from the present sample and open symbols are the stars from L07. The symbols for the 18 stars in common are connected. Dotted drop lines show the correction for comparison star variation. (b) Mean chromospheric Ca H+K activity vs. photometric $(b + y)/2$ brightness variation (linear scale). The dashed line is the transformed power law, and the dotted line is the best-fit linear regression. Dotted drop lines show the correction for comparison star variation. (c) Mean chromospheric Ca H+K activity vs. photometric $(b + y)/2$ brightness variation for low-activity stars only (linear scale). The dashed line is the transformed power law, and the dotted line is the best-fit linear regression.

young, active stars, whose photometric variability is strongly spot dominated (leading invariably to a negative correlation with the chromospheric Ca II H+K variability on rotational as well as longer timescales), and older, less active stars, including the Sun, whose photometric behavior tends to be facula dominated (positive correlation with chromospheric variation), at least on the decadal timescale of the activity cycle. This pattern persists in the present sample.

We illustrate this behavior in Figure 14, which show the L07 sample (Figure 14(a)) and the current sample (Figures 14(b) and 14(c)). Open symbols are used to represent stars that become brighter as their H+K emission increases on the year-to-year timescale, and filled symbols represent stars that become fainter as their H+K emission increases. The size of each symbol indicates the significance of the correlation. The dividing line between correlated and anticorrelated behavior falls near $\log R'_{\mathrm{HK}} = -4.65$ (L07 sample) or perhaps a bit lower, near $\log R'_{\mathrm{HK}} = -4.75$ (present sample).

The upper parts of Figures 14(a) and 14(b) are populated by young, active, relatively rapidly rotating stars that show anticorrelations exclusively, often with a high significance. Among the older, less active, more slowly rotating Sun-age stars in the lower parts of Figures 14(a) and 14(b), there seems to be a preference for a pattern of direct correlation between photometric and chromospheric emission variations, although there is an admixture of anticorrelations. Figure 14(c), the inset from Figure 14(b), shows this in more detail. One of these less active stars among those with high significance ($p < 0.05$) correlations, HD 143761, switched its allegiance between the two samples. Upon closer examination, it seems likely that this star is one for which the SSS camera changeover in 2008 affected the result: when only data from 2008–2016 (the "CCD-2" era) are analyzed, the moderately significant direct correlation becomes a low-significance anticorrelation. This example serves as a reminder that results can be instrumental (or even statistical) in origin, even at nominally high levels of significance.

The location of the dividing line between spot-dominated young stars and facula-dominated older stars corresponds fairly well to the location of the Vaughan–Preston gap (Vaughan & Preston 1980), which marks the relative absence of F-K stars with intermediate levels of magnetic activity. Although the nature and even the reality of this gap have been debated over the years (as an early example, see Hartmann et al. 1984), it has

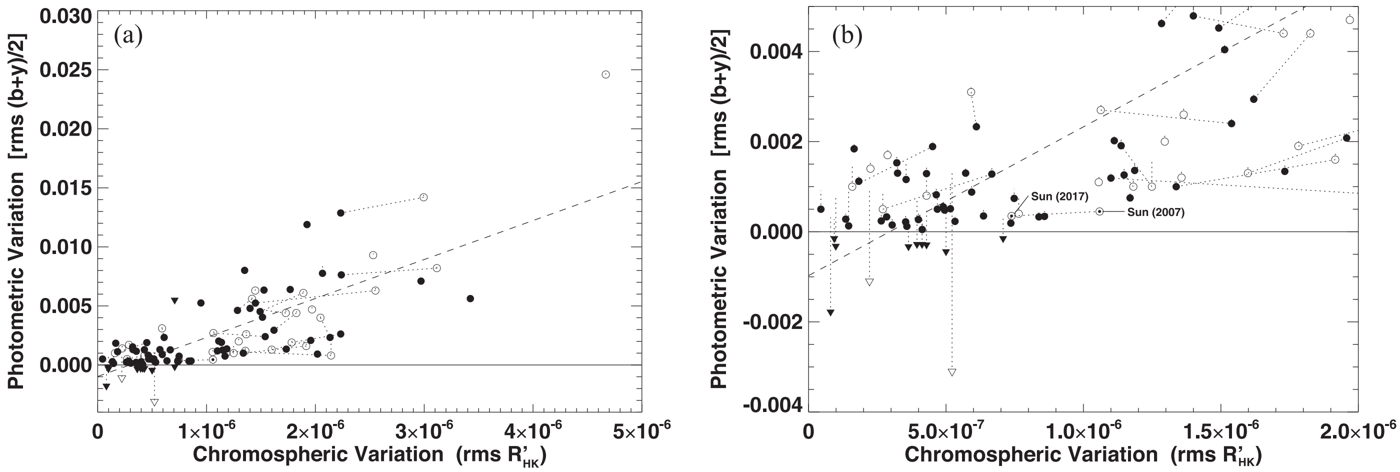

Figure 13. (a) Chromospheric Ca H+K emission variation vs. photometric $(b + y)/2$ brightness variation (linear scale). Filled symbols are stars from the present sample, open symbols are the stars from L07, and the symbols for the 18 stars in common are connected. Dotted drop lines show the correction for comparison star variation. (b) Chromospheric Ca H+K emission variation vs. photometric $(b + y)/2$ brightness variation for low-variability stars (linear scale).

been resilient. It corresponds to a rotation period of about 17 days for G-type stars (shorter (~12 days) for F-type stars and longer (~26 days) for K-type stars; Metcalfe et al. 2016), and an age of perhaps 2.5 Gyr for a solar-type dwarf (Mamajek & Hillenbrand 2008). Our results suggest that the Vaughan–Preston gap may also mark the transition from spot-dominated to facula-dominated variability on the activity cycle timescale for Sun-like stars.

5.5. Regression Slope Versus Mean Activity

Figure 15 shows the slope of the regression of the annualized photometric brightness variability on annualized chromospheric emission variability, as a function of mean chromospheric activity. As in Figures 11–13, the filled symbols are stars from the present sample, the open symbols are the stars from L07, and the symbols for the 18 stars in common are connected. The dashed line is a LOWESS fit to the data with a fairly broad width parameter of 35 (i.e., about $1/2$). The detailed appearance of a LOWESS fit is fairly sensitive to the value chosen for this parameter, so the particular curve shown should be regarded as only one from a family of possible curves; we show it simply to convey a qualitative impression of the run of the slopes as a function of average activity. The error bars are the standard errors of the regression slopes, and we have plotted them for only 20% of the stars to avoid clutter. On the left side of the diagram, it is easy to spot HD 143761, discussed previously, with its switch between negative and positive slope.

Figure 15 reinforces our conclusion that the year-to-year photometric variability of young, active stars—those with log $R'_{\mathrm{HK}} > -4.75$, perhaps—is driven by dark spots. A few such stars (e.g., HD 35296 and HD 39587, which are common to both samples) fall near the zero-slope line at least once; this fact and length of the error bars both suggest that active stars may occasionally cross it. In contrast, older, more Sun-age stars appear to be genuinely distributed on both sides of the zero-slope line, and may indeed cross back and forth as the balance between spot dimming and facular brightening changes and evolves. Although the present-day Sun is above the zero-slope line, its location there may not be forever unchanging.

A study of photometric data from *Kepler* (Montet et al. 2017) for stars with presumptive spectral types F7 to G4 shows year-to-year brightness variability at the 3σ level for 463 of the 3845 stars studied, with typical amplitudes of a few tenths of a percent. The detected year-to-year variability is anticorrelated with rotational modulation for rapidly rotating stars and directly correlated for more slowly rotating stars, with a gradual but ultimately complete transition that crosses over at 24 days. This behavior is attributed to spot-dominated activity for the more rapidly rotating stars, and to facula-dominated activity for the slower rotators. The lack of contextual Ca II H+K observations for the *Kepler* stars handicaps our ability to compare this *Kepler* study with ours; among nearby field stars, a rotation period of 24 days would correspond to log $R'_{\mathrm{HK}} \sim -4.8$ or -4.9, perhaps a bit lower than the crossover that we find (log $R'_{\mathrm{HK}} \sim -4.75$). Currently, there seems to be little else that we can add. The eventual accession of contextual data for stars observed by *Kepler* will definitely be welcomed.

5.6. The Relationship Between Strömgren b and Strömgren y Variability

We have previously remarked in passing (e.g., L07) that the variation in annualized magnitudes in the Strömgren b filter, σ_b, consistently exceeds that in the y filter, σ_b, by 10%–15% for Sun-like stars at all chromospheric activity levels, noting that the effect is consistent with a simple thermal blackbody interpretation of spots and faculae. In contrast, early results from *SORCE*/SIM (Haigh et al. 2010) indicated essentially no variation in a narrow spectral region centered on Strömgren b in 2004–2007, implying that σ_b/σ_y is nearly zero for the Sun. More recently, Shapiro et al. (2016), using the "SATIRE-S" model, determined that the cyclic variations of the Sun in Strömgren b is about half that in Strömgren y (their Figure 3). These results have prompted us to examine this question more carefully using the current observations.

Direct analysis of the Version 23 *SORCE*/SIM data indicates that the σ_b/σ_y ratio is 0.73 for the Sun (Section 4.2), which may be regarded as superseding the previous Haigh et al. (2010) result, and also as roughly consistent with the SATIRE-S result. The ratio is also defined for 63 of the 72 stars in our sample (i.e., those with a positive net variance in both colors); the data

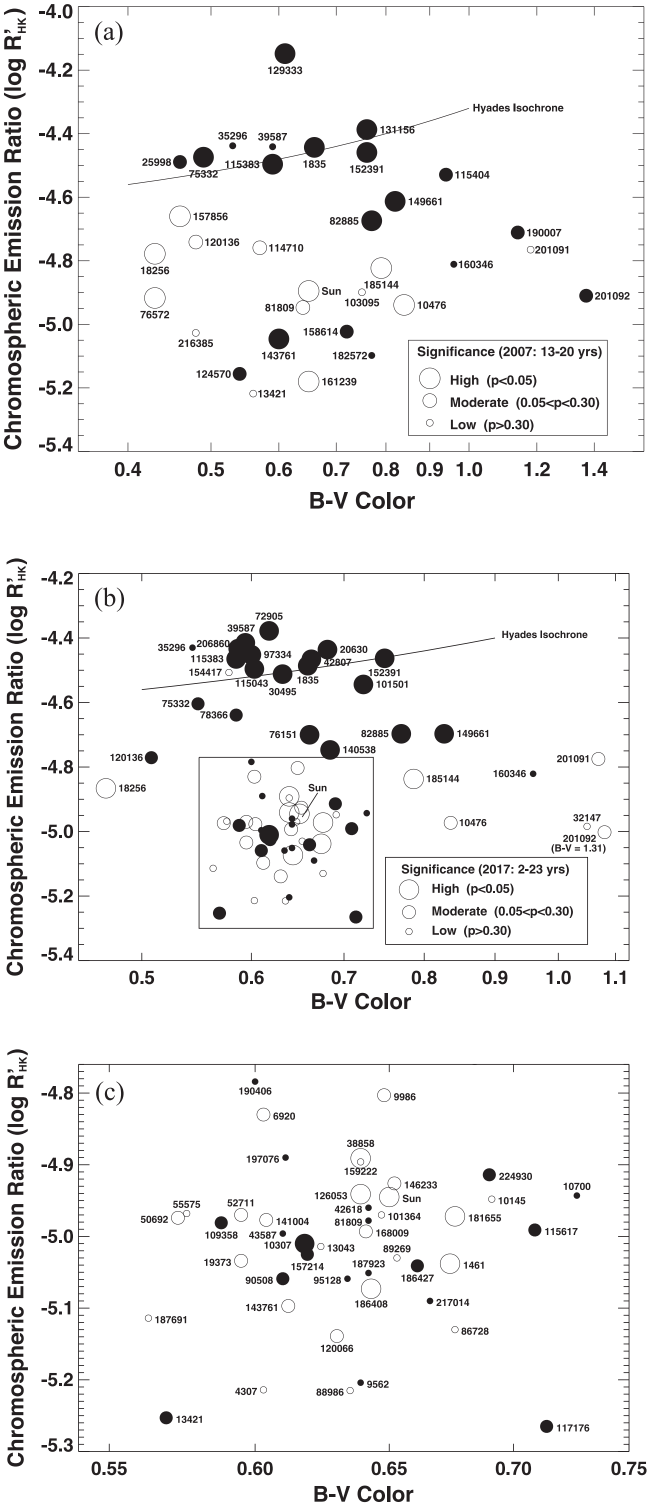

Figure 14. (a) Correlations between brightness and chromospheric variation on the year-to-year timescale (L07). (b) Correlations between brightness and chromospheric variation on the year-to-year timescale (present sample). (c) The inset from (b).

are displayed in Figure 16. The dashed line is a LOWESS fit to the data with a fairly broad width parameter of about 2/3. The mean value for σ_b/σ_y is 1.15 for all 64 stars, including the Sun. The ratio is 1.13 for the 14 tightly bunched active stars with log $R'_{\rm HK} > -4.6$, and 1.16 for the more scattered less-active stars with log $R'_{\rm HK} < -4.6$, where the increased scatter probably reflects mainly the relatively larger errors in both the numerator and the denominator of the ratio. For the solar twin 18 Sco (HD 146233), the ratio is 1.70. A similar analysis for the mainly F-type comparison stars shows that the ratio ranges from −0.95 to 1.05 for these essentially quiescent (i.e., generally nondetectably variable) stars, as would be expected. Accordingly, we conclude that our present data tend to confirm our previous impression; for Sun-like stars, the variation in Strömgren *b* typically exceeds the variation in Strömgren *y* by about 15%.

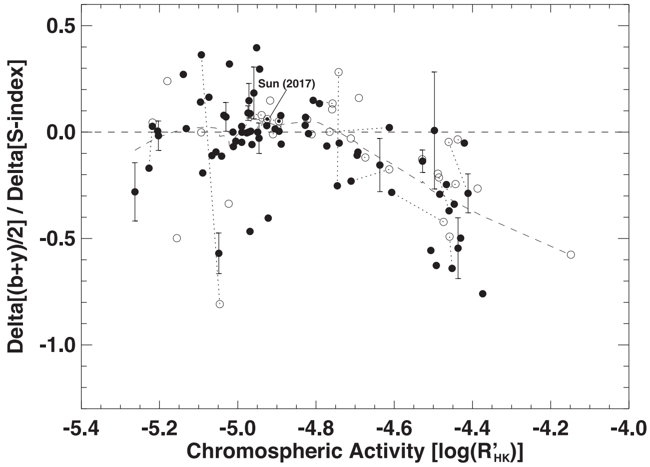

Figure 15. Slope of the regression of the photometric brightness variation on the chromospheric Ca II H+K emission variation, plotted as a function of average chromospheric emission. Filled symbols are stars from the present sample, open symbols are the stars from L07, and the symbols for the 18 stars in common are connected. The dashed line is a LOWESS fit to the data.

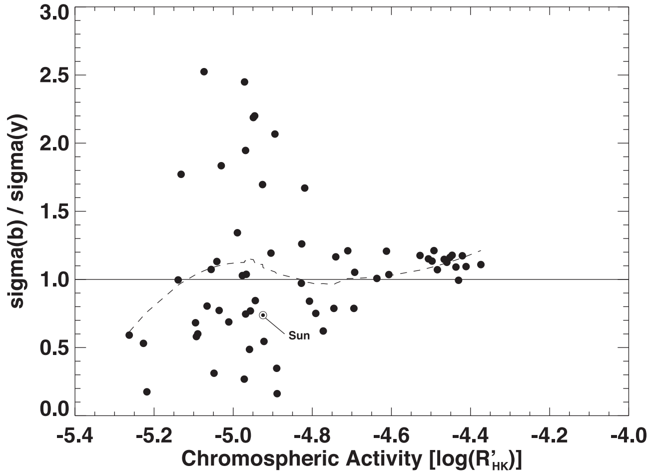

Figure 16. Ratio σ_b/σ_y as a function of log $R'_{\rm HK}$. The dashed line is a LOWESS fit to the data.

5.7. Comments on Specific Stars

5.7.1. HD 146233 = 18 Sco (The "Solar Twin")

The G2V star HD 146233 (18 Sco) became a target for the Lowell SSS program in 1995, even before it was identified as a near-perfect "solar twin" (Porto de Mello & da Silva 1997), and APT photometry at Fairborn began in 2000. With now a total of 17 years of joint observation, 18 Sco's activity cycle is known to vary directly in chromospheric S-index emission and photometric b, y brightness (Figure 4(c)). From a few early MWO H+K observations plus the 1995–2016 Lowell SSS data, the activity cycle is known to be multi-timescale, with a principal period of 14.0 years and a secondary of 6.5 years (Egeland 2016). Both the S-index variation and the photometric variation of 18 Sco are not too dissimilar to those of the Sun. The status of 18 Sco as a “solar twin” remains secure.

5.7.2. HD 81809, a Puzzling Subgiant

Our sample includes the subgiant HD 81809. This star is a “line-width spectroscopic binary” (Pourbaix 2000) with a visual orbit and a *Hipparcos* parallax, so its component masses and luminosities are known: the masses are 1.7 ± 0.6 and 1.0 ± 0.2, and the system’s absolute magnitude is 2.98, which places it squarely on the subgiant branch. The magnitude difference for the components is variously given as 1.0–1.5. The star (or, more precisely, one of its components) also has a simple, regular, ~8 year Sun-like activity cycle that has attracted considerable attention (it is the “Sun-like cycle” star immediately adjacent to the Sun in Figure 2, and one of the cluster of “Sun-like cycle” stars near the Sun in Figure 5). Consequently, it is now also known that the X-ray luminosity of HD 81809 is about 30× that of the Sun, and that this emission follows the activity cycle (Favata et al. 2008).

Upon closer consideration, HD 81809 is also a bit of a puzzle. The primary is indisputably evolved, and its main sequence progenitor was presumably an A- or F-type star (most likely an early F-type star), with a main-sequence lifetime of 1–3 Gyr. The comparatively vigorous X-ray activity is also consistent with an age considerably younger than the Sun. The secondary is presumably a G-type star that has not yet had time to evolve significantly, yet its inferred absolute magnitude is about 4.1, which places it well above the main sequence. Which component is the cycling star is also unclear. On one hand, it is difficult to model the vigorous X-ray emission in terms of Sun-like magnetic features unless the active star is the primary—there simply is not enough surface area available on the secondary (Favata et al. 2008). (This argument, however, ignores the fact that young, main-sequence solar-type stars—in the Hyades, for example—manage to produce even more X-ray emission than does HD 81809 without the benefit of additional surface area: the reason being, presumably, that the X-ray emission mechanism for young stars is not strictly Sun-like. Obviously, this might be true for the active component of HD 81809, also.) In contrast, the conventional wisdom that subgiants are inactive could suggest that the cycling star is the secondary, although Wright (2004) pointed out simply that profoundly inactive stars are subgiants, and not necessarily the converse.

Our present results show that HD 81809 is clearly variable (Table 2 and Figure 4.31), and that the photometric variations are weakly anticorrelated with its H+K variations (Figure 14(c)). What is beyond dispute is that, photometrically, we are mainly watching the variation of the primary star, proving that subgiants can, indeed, be variable. If the cycling (and X-ray emitting) component of HD 81809 is the primary, we have the puzzle of explaining why the correlation that exists so clearly between chromospheric H+K emission and X-ray variability breaks down when photometry is added to the mix. If the secondary is the active star, the lack of correlation between photometric and H+K variability is a non-issue, simply because two different stars are involved, but there are other problems. In particular, the S-index, which is the line core emission in H&K normalized by the flux in the nearby pseudo-continuum, would be a hybrid, the line core emission coming mainly from the secondary, but the normalizing flux from the primary. The consequence is that the measured S-index and the derived value for R'_{HK} would be deceptively low, perhaps by as much as 0.5 dex in R'_{HK}. Adjustment by this amount would propel the active star, now presumptively the secondary, into the regime of young, active, Hyades-age stars (cf., Figure 14(b)) and, while HD 81809 is almost certainly younger than the Sun, it seems a bit of a stretch to argue that it is Hyades’ age (i.e., ~0.6 Gyr) or even younger. An age of 1 Gyr or a bit more, however, could explain its relatively vigorous X-ray emission.

5.7.3. HD 140538 = ψ Ser, a Star Apparently Emerging from Flat Activity

The star HD 140538 (ψ Ser), added to the Lowell SSS program in 1997, showed several years of essentially flat H+K emission, followed in year 2000 by the onset of cycles of steadily increasing amplitude in both H+K emission and $(b + y)/2$ photometry, with a cycle period of about four years. In fact, the APT photometry began four years earlier, in 1993, and suggests that the relatively quiescent behavior of the star that ended around year 2000 extended back to 1993 (Figure 4.49). With $\log R'_{\mathrm{HK}} = -4.73$ and spectral type G2.5V, ψ Ser is somewhat younger and more active than the Sun.

5.7.4. HD 186408 = 16 Cyg A, Possibly a New Candidate for “Most Sun-like” Star

The referee found our remark in the caption of Figure 5, where we judged HD 186408 (16 Cyg A) to be a star with a simple Sun-like activity cycle, to be of some interest, prompting us to take a closer look ourselves. The origin of our judgment is the appearance of the stackplot for that star (Figure 4.62). The SSS data from 2004–2016 (seasons 13–25 on the stackplot), much of it from the CCD-2 era, certainly create the impression that HD 186408 has executed a cycle some 10–12 years long during those years, and the APT photometry appears to confirm it, albeit in the face of substantial noise from the comparison stars. It is, of course, a bit presumptuous to claim a 10–12 year activity cycle from the subjective appearance of two 13 year time series; confirmation from further observations is surely needed.

However, if HD 186408 does, indeed, have a smooth, Sun-like activity cycle 10–12 years long, it becomes a very interesting star, because it also has a Sun-like rotation period of 23.8 days (Davies et al. 2015), derived from asteroseismic observations from the *Kepler* spacecraft. It would land right next to the Sun in the Böhm-Vitense diagram, midway between the “A” and “I” branches (Böhm-Vitense 2007; Metcalfe et al. 2016), where the Sun now resides in splendid isolation—the Sun would no longer be quite so unique.

6. Summary and Conclusions

After nearly 35 years of study, what do we know about the patterns of variation for the Sun and Sun-like stars that we did not know at the outset?

First of all, it is incredibly hard to achieve and maintain the precision needed in the stellar observations to make the comparison between solar and stellar behavior, at least using ground-based photometry. There will probably never be stellar time series with the duration, dense coverage, and the astounding photometric precision of the solar observations shown in Figure 1 for many, or perhaps even any, Sun-like stars, absent a dedicated, coordinated, long-term ground- and space-mission to obtain the needed spectroscopic and photometric data.

The precision achievable from photoelectric photometry with a meter-class APT is about 0.1% for a single (nightly) observation. In comparison, a solar radiometer like *SORCE*/TIM achieves a daily precision better than 0.001% (100× better), and the *Kepler* CCD imagery achieves a daily photometric precision of about 0.01% (10× better) by maintaining subpixel pointing. Although these numbers are only approximate, they frame the issue.

For ground-based photometry, the problem is how to achieve 10× – 100× better precision than APT photometry currently does, and the prospects for this are not good. The error budgets for APT photoelectric photometry and ground-based CCD photometry both contain dominant terms that start coming strongly into play at precisions between 1% and 0.1%; for APT photometry, it is variable comparison stars, and for ground-based CCD photometry, it is flat-fielding. Variable seeing implies a variable PSF, so the *Kepler* trick of sidestepping the flat-fielding problem by maintaining precise subpixel registration is likely unavailable in ground-based work with CCDs. Larger telescopes would not help much, and might actually be a hindrance in practice due to competition for observing time.

For space-based photometry, the needed precision is, of course, achievable; the constraints are mission cost and duration: space missions are expensive, and they tend to have lifetimes of years, not decades, although *Hubble* and *SOHO* have certainly been exceptions to the latter rule. Accordingly, space-based research on stellar activity cycles will probably continue to piggyback on missions with other primary objectives, as with *Kepler*. In this respect, the Transiting Exoplanet Survey Satellite (*TESS*) mission comes to mind, but here there will be a serious timescale mismatch: *TESS* will observe any given field for only about a month before moving on to another field in its two-year mission, and a month is much too short to characterize stellar cycles that last for years or even decades—even two years would not be enough. Asteroseimology using *TESS* data will face the same mismatch; we know from helioseismology that the Sun's oscillation frequency spectrum responds to the solar cycle, but we know this only because helioseimic observations of the Sun now extend over a couple of solar cycles.

For Ca II H+K spectroscopy, telescope aperture is certainly important; the 1.1 m telescope that hosts SSS, for example, is definitely a limitation to the SSS program. Thus, an instrument like the fiber-coupled Potsdam Echelle Polarimetric and Spectroscopic Instrument (PEPSI) operating at the 2 × 8.4 m Large Binocular Telescope (LBT) would certainly be splendidly suited for obtaining long-term Ca II H+K observations for both the Sun and Sun-like stars, but, once again, the challenge would be successfully competing for observing time over years or even decades.

Whatever the prospects for future efforts in solar-stellar cycle research, the principal conclusions we arrived at 20 years ago still stand, namely: (1) both chromospheric H+K and photometric b, y variability on the year-to-year timescale among Sun-like stars are related to the average chromospheric activity by power laws. (2) On the year-to-year timescale and longer, young active stars become fainter as their H+K emission increases. This implies that the photometric variability of young stars is dominated by dark spots on these timescales, unlike the Sun, where facular emission dominates. (3) Among older, less active, Sun-age stars, a pattern of direct correlation between photometric and chromospheric emission variations, not unlike the pattern between TSI and Ca II K-index variations shown by the Sun, occurs as a common, albeit not a universal, behavior. Finally, although the Sun does not appear to differ strongly from its stellar age and spectral class mates in the activity and variability characteristics that we have now been studying for over three decades, there remains the lingering impression that it may be unusual in two respects: (1) its comparatively smooth, regular activity cycle, and (2) its rather low photometric brightness variation relative to its chromospheric activity level and variation, perhaps indicating that facular emission and sunspot darkening are especially well-balanced on the Sun.

The authors thank Lou Boyd of Fairborn Observatory and Brian Skiff and Len Bright of Lowell Observatory for their years of crucial support to the APT and SSS programs. R.R.R. thanks the National Solar Observatory for support as an Emeritus Astronomer. G.W.L. thanks Lowell Observatory for informal emeritus status, access to facilities, and travel support in continuing post-retirement stellar research. G.W.H. acknowledges long-term support from NASA, NSF, Tennessee State University, and the State of Tennessee through its Centers of Excellence program. The referee's careful reading and knowledgeable comments enabled us to improve the overall scholarship of our paper and expand our discussion of the results, and we appreciate that anonymous contribution. This research utilized data courtesy of NASA/*SORCE* and the SIM and TIM science teams, and SOLIS data obtained by the NSO Integrated Synoptic Program (NISP), managed by the National Solar Observatory, which is operated by the Association of Universities for Research in Astronomy (AURA), Inc. under a cooperative agreement with the National Science Foundation. This research has made use of the SIMBAD database and its VizieR catalog access tool, especially the catalog of MK spectral types (B/mk/mktypes) created and maintained by Brian Skiff of Lowell Observatory. SIMBAD and VizierR are operated at CDS, Strasbourg, France (Wenger et al. 2000). For the two lead authors, this paper will likely be our final word on this subject.

ORCID iDs

Gregory W. Henry https://orcid.org/0000-0003-4155-8513
Alexei A. Pevtsov https://orcid.org/0000-0003-0489-0920

References

Anderson, D. E., & Cahalan, R. E. 2005, SoPh, 230, 3
Baliunas, S. L., Donahue, R. A., Soon, W. H., et al. 1995, ApJ, 438, 269
Baliunas, S. L., Donahue, R. A., Soon, W. H., & Henry, G. W. 1998, in ASP Conf. Ser. 154, Cool Stars, Stellar Systems and the Sun, ed. R. A. Donahue & J. A. Bookbinder (San Francisco, CA: ASP), 153
Ball, W. T., Unruh, Y. C., Krivova, N. A., Solanki, S., & Harder, J. W. 2011, A&A, 530, 71
Bertello, L., Pevtsov, A. A., Harvey, J. W., & Toussaint, R. M. 2011, SoPh, 272, 229
Böhm-Vitense, E. 2007, ApJ, 657, 486
Cayrel de Strobel, G. 1996, A&ARv, 7, 243

Chugainov, P. F. 1966, IBVS, 122, 1
Criscuoli, S., & Uitenbroek, H. 2014, ApJ, 788, 151
Davies, G. R., Chaplin, W. J., Farr, W. M., et al. 2015, MNRAS, 446, 2959
Eaton, J. A., & Hall, D. S. 1979, ApJ, 227, 907
Egeland, R. 2016, presentation given at Cool Stars 19 Monday Morning Plenary Session, http://schwab.tsuniv.edu/papers/cs19/cs19_talk2.pdf
Egeland, R., Metcalfe, T. S., Hall, J. C., & Henry, G. W. 2015, ApJ, 812, 12
Egeland, R., Soon, W., Baliunas, S., Hall, J. C., & Henry, G. W. 2017a, in IAU Sym. 328, Living around Active Stars, ed. D. Nandy, A. Valio, & P. Petit (Cambridge: Cambridge University Press), 329
Egeland, R., Soon, W., Baliunas, S., et al. 2017b, ApJ, 835, 25
Eggen, O. J. 1986, AJ, 92, 910
ESA 1997, The Hipparcos and Tycho Catalogues, ESA SP–1200 (Noordwijk: European Space Agency)
Favata, F., Micela, G., Orlando, S., et al. 2008, A&A, 490, 1121
Foukal, P., Little, R., Graves, J., Rabin, D., & Lynch, D. 1990, ApJ, 353, 712
Grenon, M. 1993, in ASP Conf. Ser. 40, Inside the Stars, ed. W. Weiss & A. Baglin (San Francisco, CA: ASP), 693
Haigh, J. D., Winning, A. R., Toumi, R., & Harder, J. W. 2010, Natur, 467, 696
Hall, J. C., Henry, G. W., & Lockwood, G. W. 2007a, AJ, 133, 2206
Hall, J. C., Henry, G. W., Lockwood, G. W., Skiff, B. A., & Saar, S. H. 2009, AJ, 138, 312
Hall, J. C., & Lockwood, G. W. 1995, ApJ, 438, 404
Hall, J. C., Lockwood, G. W., & Skiff, B. A. 2007b, AJ, 133, 862
Harder, J. W., Fontenla, J. M., Pilewskie, P., Richard, E. C., & Woods, T. N. 2009, GRL, 36, L07801
Hartmann, L., Soderblom, D. R., Noyes, R. W., & Burnham, N. 1984, ApJ, 276, 254
Hauck, B., & Mermilliod, M. 1998, A&AS, 129, 431
Henry, G. W. 1999, PASP, 111, 845
Jerzykiewicz, M., & Serkowski, K. 1966, LowOB, 6, 295
Johnson, H. L., Mitchell, R. I., Iriarte, B., & Wisniewski, W. Z. 1966, CoLPL, 4, 99
Judge, P. G., Carlsson, M., & Stein, R. F. 2003, ApJ, 597, 1158
Judge, P. G., Lockwood, G. W., Radick, R. R., et al. 2012, A&A, 544, A88
Karoff, C., Metcalfe, T. S., Santos, A. R. G., et al. 2018, ApJ, 852, 46
Knaack, R., Fligge, M., Solanki, S. K., & Unruh, Y. C. 2001, A&A, 376, 1080
Kron, G. E. 1950, AJ, 55, 69
Lean, J. L. 2000, GRL, 27, 2425
Lockwood, G. W., Henry, G. W., Hall, J. C., & Radick, R. R. 2013, in ASP Conf. Ser. 472, New Quests in Stellar Astrophysics III: A Panchromatic View of Solar Like Stars With and Without Planets, ed. M. Chavez et al. (San Francisco, CA: ASP), 203
Lockwood, G. W., Skiff, B. A., Henry, G. W., et al. 2007, ApJS, 171, 260
Lockwood, G. W., Skiff, B. A., & Radick, R. R. 1997, ApJ, 485, 789
Lockwood, G. W., Thompson, D. T., Radick, R. R., et al. 1984, PASP, 96, 714
Mamajek, E. E., & Hillenbrand, L. A. 2008, ApJ, 687, 1264
McQuillan, A., Mazeh, T., & Aigrain, S. 2014, ApJS, 211, 24
Metcalfe, T. S., Egeland, R., & van Saders, J. 2016, ApJL, 723, L213
Middelkoop, F. 1982, A&A, 107, 31
Montet, B. T., Tovar, G., & Foreman-Mackey, D. 2017, ApJ, 851, 116
Noyes, R. W., Hartmann, L. W., Baliunas, S. L., et al. 1984, ApJ, 279, 763
Oláh, K., Kővári, Zs., Petrovay, K., et al. 2016, A&A, 590, 133
Olsen, E. H. 1993, A&AS, 102, 89
Olsen, E. H. 1994a, A&AS, 104, 429
Olsen, E. H. 1994b, A&AS, 106, 257
Pevtsov, A. A., Bertello, L., & Uitenbroek, H. 2013, ApJ, 767, 56
Porto de Mello, G. F., & da Silva, L. 1997, ApJ, 482, L89
Pourbaix, D. 2000, A&AS, 145, 215
Preminger, D. G., Chapman, G. A., & Cookson, A. M. 2011, ApJ, 739, L45
Radick, R. R., Lockwood, G. W., Skiff, B. A., & Baliunas, S. L. 1998, ApJS, 118, 239
Radick, R. R., Lockwood, G. W., Skiff, B. A., & Thompson, D. T. 1995, ApJ, 452, 332
Radick, R. R., Skiff, B. A., & Lockwood, G. W. 1990, ApJ, 353, 524
Radick, R. R., Thompson, D. T., Lockwood, G. W., et al. 1987, ApJ, 321, 459
Rosenberger, J. L., & Gasko, M. 1982, in Understanding Robust and Exploratory Data Analysis, ed. D. C. Hoaglin, F. Mosteller, & J. W. Tukey (New York: Wiley), 195
Rutten, R. G. M. 1984, A&A, 130, 353
Scargle, J. D., Keil, S. L., & Worden, S. P. 2013, ApJ, 771, 33
Schrijver, C. J. 1995, A&ARv, 6, 181
Shapiro, A. I., Solanki, S. K., Krivova, N. A., Tagirov, R. V., & Schmutz, W. K. 2015, A&A, 581, A116
Shapiro, A. I., Solanki, S. K., Krivova, N. A., Yeo, K. L., & Schmutz, W. K. 2016, A&A, 589, A46
Shapiro, A. I., Solanki, S. K., Krivova, N. A., et al. 2014, A&A, 569, A38
Soderblom, D. R., & King, J. R. 1998, in Solar Analogs: Characteristics and Optimum Candidates, ed. J. C. Hall (Flagstaff, AZ: Lowell Observatory), 41
Soubiran, C., & Triaud, A. 2004, A&A, 418, 1089
Struve, O. 1946, AnAp, 9, 1
Torres, C. A. O., & Ferraz Mello, S. 1973, A&A, 27, 231
Vaughan, A. H., & Preston, G. W. 1980, PASP, 92, 385
Wehrli, C., Schmutz, W., & Shapiro, A. I. 2013, A&A, 556, L3
Wenger, M., Ochsenbein, F., Egret, D., et al. 2000, A&AS, 143, 9
White, O. R., Livingston, W. C., Keil, S. L., & Henry, T. W. 1998, in ASP Conf. Ser. 140, Synoptic Solar Physics, ed. K. S. Balasubramaniam, J. Harvey, & D. Rabin (San Francisco, CA: ASP), 293
Wilson, O. C. 1978, ApJ, 226, 379
Woods, T. N., Snow, M., Harder, J., Chapman, G., & Cookson, A. 2015, SoPh, 290, 2649
Wright, J. T. 2004, AJ, 128, 1273